TECHNISCHE UNIVERSITÄT WIEN
Vienna University of Technology

DIPLOMARBEIT

Impedance spectroscopic characterization of ceria based anodes for solid oxide fuel cells

Ausgeführt am Institut für Chemische Technologien und Analytik, Fachbereich Elektrochemie der Technischen Universität Wien

Unter der Anleitung von

Univ. Prof. Dipl.-Phys. Dr. Jürgen Fleig

Univ.Ass. Dipl.-Ing. Dr.techn. Alexander Opitz

Dipl.-Ing. Andreas Nenning

durch

Peter Velicsanyi

Csengery Straße 85.

9400 Sopron, Ungarn

12. August 2014

Vorwort

Diese Arbeit entstand an der Technischen Universität Wien am Institut für Chemische Technologien und Analytik in der Forschungsgruppe Festkörperelektrochemie und keramische Materialien unter der Anleitung von Herrn Professon Jürgen Fleig.

Mein besonderer Dank gilt Professor Jürgen Fleig, der meine Arbeit in dieser Arbeitsgruppe ermöglicht und mit Hilfe und vielen netten Worten unterstützt hat. Auch seine interessanten Vorlesungen und Vorlesungsmaterialien darf man nicht vergessen, die mein Interesse für Festkörperelektrochemie geweckt haben. Außerdem möchte ich mich auch für die finanzierte Teilnahme an der „E-MRS Spring Meeting 2014“-Konferenz bedanken. Diese war ein wesentliches Erlebnis in meinem wissenschaftlichen Leben.

Mein besonderer Dank gilt auch meinen Betreuer, Andreas Nenning für die anspruchsvolle Einschulung an die Geräte, für die Hilfe in der Laborarbeit und der Auswertung/Interpretation meiner Messungen. Vielen Dank auch für die theoretischen Aspekte, ich glaube, dass ich (“als ebenso ein theoretischer Mensch“) sehr viel von ihm habe lernen können.

Ich möchte mich auch bei meinem Bürokollegen, Alexander Opitz für seinen Rat und für seine Hilfe während meiner Arbeit bedanken. Ohne seine Gedanken wären einige wichtige Messungen nicht durchgeführt worden.

Danke auch an Ghislain Rupp für die Aufnahme der XRD Spektren, an Edvinas Navickas für die SIMS-Messungen und für die Hilfe in den Tracer-Experimenten, sowie Elisabeth Eitenberger für die SEM-Aufnahmen. Danke auch an Sandra Kogler, die mir auch viel geholfen hat, z.B. mein Messschwert wäre ohne sie viel langsamer fertig geworden.

Bedanken möchte ich mich ganz besonders bei meiner Mutter, die mit ihrer bedingungslosen und hingebenden mütterlichen Liebe und Unterstützung meine Studien ermöglicht hat. Apu, ich weiss, dass du mich auch von dort...von oben sehen kannst.

Abstract

In materials research ceria is a highly interesting material owing to its attractive catalytic surface activity and it was thus intensively investigated within the last decade. This high catalytic activity was recently demonstrated to be also very beneficial for the electrochemical H_2 oxidation on Sm doped CeO_2 electrodes with noble metal current collectors. For further improvement and understanding, analysis of the effect of (co-)doping on transport and surface kinetics is helpful for the developement of ceria-based solid oxide fuel cell (SOFC) anodes.

In the present study, model-type thin films of Gd doped and Gd/Mn co-doped ceria were investigated by means of impedance spectroscopy in humid H_2 atmosphere. A novel measurement technique for microelectrodes with interdigitating Pt current collectors was employed. This method allows a separation of the different elementary processes contributing to the electrode impedance. After annealing at 650°C in humid H_2 atmosphere, there is no significant difference in the electronic resistivity between the two materials. In terms of surface exchange rate, however, the Gd/Mn co-doped ceria shows the higher catalytic activity.

In addition ^{18}O tracer incorporation into Gd-doped ceria electrodes from a $H_2/H_2^{18}O$ atmosphere was performed with and without cathodic polarization. The tracer distribution within the ceria thin film was subsequently analyzed by secondary ion mass spectrometry (SIMS) and correlated with the electrochemical results.

Kurzfassung

Die hohe Oberflächenaktivität macht Ceroxid zu einem sehr interessanten Material in der Materialforschung und ist auch die Basis vieler aktueller und zukünftiger Anwendungen. Aus diesem Grund wird es von zahlreichen Forschungsgruppen intensiv untersucht. Ein wesentlicher Punkt hierbei ist die Frage der Dotierung. Zum Beispiel wurden Sm dotierte Elektroden untersucht und erwiesen sich als aktiv für die H_2-Oxidation (Anodenreaktion in Festoxidbrennstoffzellen, SOFCs). Für die weitere Entwicklung von Ceroxid-basierten Anodenmaterialien für SOFCs spielt die Analyse der Eigenschaften bei (Co-)Dotierung eine entscheidende Rolle.

In dieser Arbeit wurden Dünnschichtelektroden aus Gd dotiertem und Gd/Mn co-dotiertem Ceroxid mittels Impedanzspektroskopie in reduzierender Atmosphäre untersucht. Eine neue Messtechnik für Mikroelektroden mit Pt-Stromsammlern wurde eingesetzt, welche die Trennung der unterschiedlichen Elementarprozesse, die zum Impedanzspektrum beitragen, ermöglicht. Mit dieser Messmethode wurde nach Aufheizen bis 650 °C in befeuchteter H_2 Atmosphäre in der elektronischen Leitfähigkeit kein signifikanter Unterschied gefunden, während bezüglich der Oberflächenaktivität das Gd/Mn co-dotiertes Material besser zu sein scheint.

Zusätzlich wurden auch Tracer-Experimente durchgeführt, mit denen der Einbau von ^{18}O aus einer $H_2/H_2^{18}O$-Atmosphäre untersucht wurde, entweder ohne oder mit kathodischer Polarisation der Elektrode. Nach dem Experiment wurde die ^{18}O-Verteilung mit Hilfe eines Flugzeit-Sekundärionenmassenspektrometers gemessen und die Ergebnisse wurden

mit denen aus den elektrochemischen Messungen verglichen.

Contents

Chapter 1

Introduction

In our society, the interest in clean and sustainable energy becomes higher and higher. Solid oxide fuel cell (SOFC) technology is a potential candidate for enabling efficient power generation [1], consequently the importance in searching and developing advanced SOFC materials has been increasing in recent years with the intention to produce alternative energy with high efficiency at lower price. Compared to other fuel cell technologies, the use of a solid electrolyte material makes it possible to avoid corrosive environments. Also the high flexibility of operation makes SOFCs suitable for taking a share of future power generation in a wide range of applications including stationary and mobile devices.

Solid oxide fuel cells are electrochemical energy conversion devices, which produce electric current by oxidizing a fuel. This fuel can be hydrogen, but an appropriate choice of electrode and electrolyte materials allows a variety of hydrocarbons to be utilized. The current production from hydrogen is based on the reactions shown in Figure 1.1. As it can be seen, on the anode hydrogen (or fuel) is oxidised, on the cathode oxygen is reduced, while oxygen ions are transported through a solid electrolyte. The driving force for these processes is the different oxygen partial pressures on the two sides. The appropriate choice of the materials used for SOFCs is of crucial importance for efficient operation. A suitable electrolyte material is an ionic conductor with no (or very low) electronic conductivity,

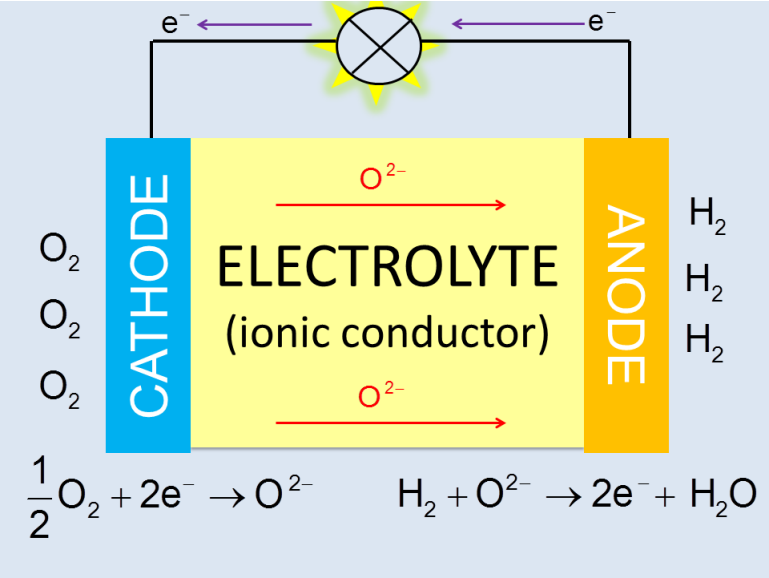

Figure 1.1: Basic principle of a solid oxide fuel cell

while the electrode materials should exhibit good electronic conductivity, so that they can make the conversion between electronic and ionic current possible.

The total reaction occuring in an SOFC is water synthesis:

$$\mathrm{H_2} + \frac{1}{2}\mathrm{O_2} \longrightarrow \mathrm{H_2O} \tag{1.1}$$

The highest possible electric energy from a SOFC is the change in the standard free enthalpy (Gibbs energy) of the reaction:

$$\Delta_\mathrm{r} G = -zFU_\mathrm{cell} \tag{1.2}$$

On the right hand side one can see the useful electric work, where z is the number of elementary charge carriers in the reaction, $F = 96485\ \frac{\mathrm{C}}{\mathrm{mol}}$ the Faraday-constant, U_cell is the cell voltage. The negative sign expresses the convention used in thermodynamics, on the basis of which the work of a system on its enviroment is negative.

However, U_cell is the open circuit voltage. If current is flowing, the measured voltage is always lower than U_cell, since there are some resistive processes in the system. This can be separated into three main parts: voltage losses in the electrolyte (ionic resistivity), anode and cathode (ionic, electronic resistivity, reactions etc.).

In SOFCs the most widely used electrolyte material is yttria stabilised zirconia [2] (YSZ). The doping of pure zirconia (ZrO_2) with yttria (Y_2O_3) provides some Y^{3+} ions at Zr^{4+} lattice sites. This means a relative negative charge in comparison to the Zr^{4+} ion (ideal situation), the consequence of which are oxygen vacancies because of the fact, that electroneutrality has to be strictly fulfilled. Since these vacancies are very mobile at higher temperatures ($T > 400 - 500\,°C$), YSZ is given its more important feature: the O^{2-} ion conductivity. Based on these facts, YSZ is well-suited to be employed in solid oxide fuel cells as an electrolyte material.

Typical cathode materials are ceramics exhibiting perovskite-type crystal structure [3], for instance, Sr doped $LaMnO_3$ (LSM), which works as cathode typically at $800 - 1000\,°C$. The reaction mechanism for oxygen reduction is not clarified yet and there are some problems with this material, such as zirconate formation at higher temperatures or poisoning effects due to interconnectors used in SOFCs. Thus, also other materials have been investigated [4], e.g. LSC ($La_{0.6}Sr_{0.4}CoO_{3-\delta}$) and LSF ($La_{0.6}Sr_{0.4}FeO_{3-\delta}$), which provide higher electronic and ionic conductivity than LSM does, while the oxygen exchange activity is also better, though, the degradation of these materials is a concern. For the future, LSCF ($La_{0.6}Sr_{0.4}Co_{0.1-0.2}Fe_{0.9-0.8}O_{3-\delta}$) is often regarded to be the most promising materials, either purely, or as a composite with doped ceria. However, the prospective applications require long time stability, good mechanic properties, totally cleared reaction mechanism etc., which raise objections to the researchers for the near future.

Presently, the standard anodic material is Ni/YSZ-Cermet in SOFCs. Cermet means a ceramic–metallic composite, here of nickel and YSZ. Although it is a state-of-the-art anode, it does not fulfill all expectations. The biggest problem is the fact, that Ni is a good catalyst for the hydrocarbon cracking reaction, which causes the poisioning (carbon deposition) of the anodic material. This disadvantage totally precludes the possibility of the direct utilization of hydrocarbon fuels (other than CH_4) [5], [6].

Owing to their remarkable catalytic activity, ceria (CeO_2) and ceria-based oxides have

been attracting the attention of material science and they have been under investigation in the recent years also as anodes of SOFCs (solid oxide fuel cells) because they seem to lower the overpotential losses for the anode reaction and, being coking-resistant and sulphur-tolerant, they could realise a more flexibel operation of SOFCs on hydrocarbon fuels [7]. These materials are e.g. Mn, Gd or Sm doped ceria [8].

In this work, gadolinium doped and manganese/gadolinium co-doped ceria were studied in thin film form in respect of various properties (surface catalytic activity, ionic and electronic conductivity, chemical capacitance, surface structure) by using various measurement methods, among others electrochemical impedance spectroscopy, scanning electron microscopy, X-Ray diffraction etc. Also tracer experiments were carried out to investigate the oxygen exchange reaction, which were analysed by secondary ion mass spectrometry. As advantages of investigating thin films (among others) the following factors can be mentioned: well-defined orientation/geometry of thin film electrodes in comparison with porous electrodes, easier characterisation of chemistry and structure by a wide range of analytical methods [9].

Chapter 2

Basics, Theory

2.1 Defects in solids, thermodynamics

Many properties of a solid are related to the materials' defect chemistry. For instance, in solid state electrochemistry electronic and ionic defects are of crucial importance, as they determine the „quality "of the corresponding conduction mechanism. In this part, we restrict ourselves to the treatment of zero-dimensional defects (point defects) in ionic solid, which can be distinguished into intrinsic and extrinsic defects [10]. Intrinsic defects are thermodynamically introduced in an ideally stoichiometric crystal at $T > 0$. Extrinsic defects are caused by doping. A high level of doping leads to a situation in which intrinsic defects can be neglected because of the predominant extrinsic defects.

It is not possible to have crystals, which are defect-free in every respect, all of them exhibit some defects, though the creation of defects is an energy-consuming process. This can be explained by the free enthalpy, defined by the expressions

$$G(T, p, N) = U + pV - TS = H - TS \tag{2.1}$$

and

$$dG = -SdT + pdV + \mu dN \tag{2.2}$$

with the natural variables: temperature T, pressure p and particle number N, and:

$$\text{entropy}: \quad S = \left(-\frac{\partial G}{\partial T}\right)_{V,N} \tag{2.3}$$

$$\text{pressure}: \quad p = \left(-\frac{\partial G}{\partial V}\right)_{T,N} \tag{2.4}$$

$$\text{chemical potential}: \quad \mu = \left(-\frac{\partial G}{\partial N}\right)_{T,p} \tag{2.5}$$

The free enthalpy must have a minimum in thermodynamic equilibrium at constant temperature and pressure. The prescence of defects increases the entropy of the crystal, ΔG for introducing some defects can be negative, and G can be minimised at a given number of defects, so also the enthalpically unfavoured process of defect formation can occur.

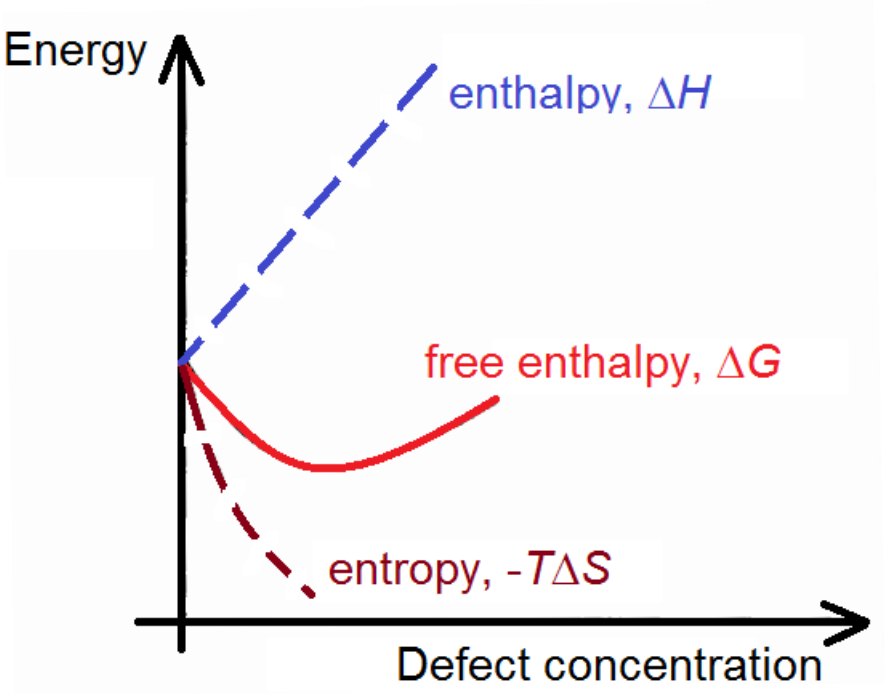

Figure 2.1: Energetic conditions in solids when introducing intrinsic defects

With these thoughts, it can be proven, that:

$$N_{\text{defect}} = N_0 \exp\left(-\frac{\Delta G^{\ominus}_{\text{defect formation}}}{kT}\right) \tag{2.6}$$

N_0 is the number of possible lattice sites and N_{defect} can express the number of *interstitals* (present atom at places which are normally not occupied), of *extra atoms*, of a *non-occupied regular place (vacancy)*. For their depiction, one can use the so called Kröger-Vink notation in the following way:

$$\mathrm{D}_{\mathrm{S}}^{\mathrm{c}} \tag{2.7}$$

Table 2.1 summarises the possible D, S and c „values“. For instance, $\mathrm{V}_{\mathrm{O}}^{\bullet\bullet}$ means an absence of an O^{2-} ion from the lattice, which is equivalent to the absence of two negative charges (so relative positive), in a simple way: oxygen vacancy. $\mathrm{Ce}_{\mathrm{Ce}}^{\prime}$ means a Ce^{3+} ion substituting a Ce^{4+} ion in the lattice, etc.

Symbol	Meaning
D	Chemical symbol of atom present, or V: vacancy
S	Where is the defect? Chemical symbol of element (lattice), i: interstitial
c	charge of the defect relative to the normal situation, $\times$: 0, $^{\bullet}$: rel.positive,$^{\prime}$: rel.negative

Table 2.1: Kröger-Vink notation

2.2 Ceria, CeO_2

Cerium(IV)-oxid, ceria is the oxide of the rare earth metal cerium and is a highly interesting material in materials research owing to the fact that it has remarkable physical and also chemical properties: among others a striking ability to store and release oxygen, which is related to a high surface catalytic activity. This property is used for present and for prospective applications. A high surface activity is also present for the hydrogen oxidation in SOFCs, occuring on the anode. According to these findings, ceria is a candidate for

anodic materials, it fullfils most expectations we have of a good electrode material. It is a good MIEC (mixed ionic and electronic conductor). This property was also investigated and confirmed in this work. These properties are related to the specific defect chemistry of ceria, which can be influenced in various ways, for instance through the atmosphere (the oxygen partial pressure), by doping, by varying temperature and so on.

Ceria crystallizes in the ideal cubic fluorite structure under ambient pressures, between room temperature and the melting point of the material, space group: F$m\bar{3}m$ [11]. In this crystal structure Ce^{4+} ions in a face-centered pattern contain a cube of O^{2-} ions. Another viewpoint: a simple cubic array of O^{2-} ions with a Ce^{4+} ion in the center of alternate cubes (Figure 2.2).

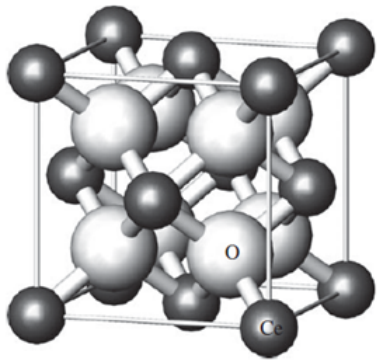

Figure 2.2: Unit cell of ceria - cubic arrangement of oxygen ions with a cerium ion in every second cube, [11]

In Figure 2.2 the unit cell of ceria can be seen. It will be important to understand this structure when investigating the effects of the crystallographic orientation on the surface catalytic activity. As it can be seen, the (100) plane contains either only Ce^{4+} or only O^{2-} ions on the surface, while in the (111) plane there are Ce^{4+} ions, as well as O^{2-} ions. According to calculations in [12] the formation energy of oxygen vacancies on CeO_2(111) surfaces is lower. Owing to the assumption, that these defects are of crucial importance for the catalytic activity for oxygen exchange, the surface orientation may strongly influence

the (electro-)catalytic activity.

2.3 Defect chemistry of ceria, doping

Ceria is a nonstoichiometric oxide, its composition can be written as $CeO_{2-\delta}$ in reducing conditions. This means, there is a permanent exchange reaction between the crystal and the atmosphere, which is in equilibrium for a given temperature and oxygen partial pressure, as Ce^{4+} can be easily reduced:

$$O_O^{\times} \longrightarrow 2e' + \frac{1}{2}O_2 + V_O^{\bullet\bullet} \tag{2.8}$$

From this equation it can be seen, that in reducing atmosphere more and more oxygen vacancies and electrons are present in the crystal which contribute to the electronic and ionic conductivity. In order to calculate the exact relationship between oxygen partial pressure and defect concentration, let us take the equilibrium constant K for this reaction:

$$K = \frac{n_{V_O^{\bullet\bullet}} n_{e'}^2}{\sqrt{p_{O_2}}} \tag{2.9}$$

Here, n_i denotes the concentration of defect i and p_{O_2} is the oxygen partial pressure. Also the charge neutrality must be strictly fulfilled:

$$2n_{V_O^{\bullet\bullet}} = n_{e'} \tag{2.10}$$

Equation (2.9) and Equation (2.10) can be rearranged to:

$$n_{V_O^{\bullet\bullet}} = \sqrt[3]{\frac{K}{4}} \sqrt[6]{\frac{1}{p_{O_2}}} \tag{2.11}$$

In logarithmic form:

$$\log n_{V_O^{\bullet\bullet}} = \text{const} - \frac{1}{6} \log p_{O_2} \tag{2.12}$$

and

$$\log n_{e'} = \text{const'} - \frac{1}{6} \log p_{O_2} \tag{2.13}$$

Therefore, the $\log n_{\text{defect}}$ vs. $\log p_{O_2}$ plot for a given temperature exhibit straight lines with a slope of $-\frac{1}{6}$. This relationship can be confirmed not only by calculation, but also by measurements. The diagram provided this way is called Brouwer diagram [13]. It is used to represent defect concentrations as a function of oxygen partial pressure (as a function of the oxidizing/reducing character of the atmosphere). The Brouwer diagram for an undoped oxide with oxygen vacancies and interstitials can be seen in Figure 2.3, [14].

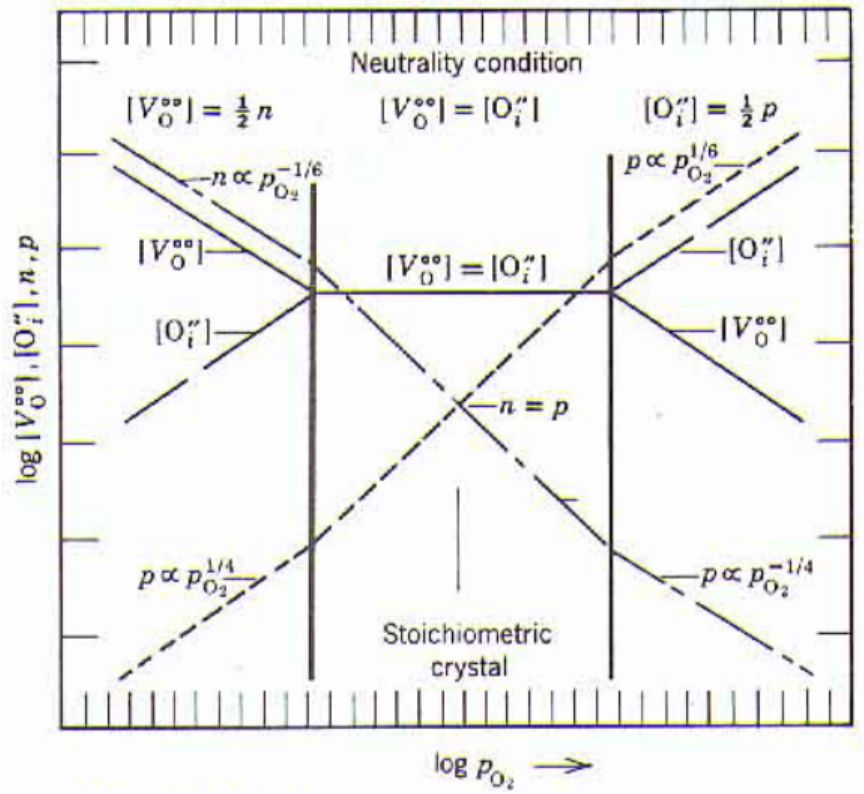

Figure 2.3: Example of the Brouwer diagram in an oxide

One can express the formation of ionic and electronic charge carriers in ceria also in the equation:

$$O_O^{\times} + Ce_{Ce}^{\times} \longrightarrow 2Ce_{Ce}' + \frac{1}{2}O_2 + V_O^{\bullet\bullet} \tag{2.14}$$

The migration process of oxygen vacancies is of high importance for the transport properties of ceria, as they are very mobile at high temperatures. In reducing atmosphere not

only these should be taken into account, but also the not nigligible electronic conduction, which becomes important under such conditions. It can be stated, that doped ceria is a good MIEC (mixed ionic and electronic conductor) material. However the ionic conductivity can be improved if a transition metal ion, whose valence is lower than +4, is introduced into ceria as a dopant [15], [16]. Therefore, it has been studied in detail, what effects some possible dopants, among others Mn, Gd, Sm can have on the behaviour of the material. This part concentrates on Gd^{3+} and Mn^{3+} as aliovalent dopants, whose introduction into ceria produces oxygen vacancies and relative negative defects (Equation (2.15), Equation (2.16)).

$$Gd_2O_3 + O_O^{\times} + 2Ce_{Ce}^{\times} \longrightarrow 2CeO_2 + Gd'_{Ce} + V_O^{\bullet\bullet} \tag{2.15}$$

$$Mn_2O_3 + O_O^{\times} + 2Ce_{Ce}^{\times} \longrightarrow 2CeO_2 + Mn'_{Ce} + V_O^{\bullet\bullet} \tag{2.16}$$

In ceria, introduction of negatively charged defects has the consequence of increasing the vacancy concentration and decreasing the intrinsic electron concentration. As it was mentioned above, due to the high amount of dopants used in many MIECs, these extrinsic defects play a major role in the material. However, the equilibrium between the gas phase and solid also remains valid (Equation (2.14) and Equation (2.9)), so the materials exhibit non-stoichiometry, as well. Therefore, e.g. the material with 20% Gd has the composition: $Gd_{0.2}Gd_{0.8}O_{1.9-\delta}$, where $O_{1.9}$ is the concentration without intrinsic defects.

2.4 Electrochemical impedance spectroscopy (EIS)

In an alternating current (AC) measurement the quantitiy corresponding to the resistance is the impedance (Z). One can say, that electrochemical impedance spectroscopy [17] means the frequency dependent measurement of the AC resistance (impedance) in an electric system. In contrast to DC measurements, in EIS measurements the individual

contributions of different conduction processes and electrochemical processes to the direct current (DC) resistance can be obtained, when a proper circuit model is available.

Ceramic materials exhibit not only conducting/semi-conducting properties, but they are also dielectrics. Therefore, in an AC circuit, two kinds of electric current flow are possible. Firstly, the transport of mobile charge carriers (electrons, ions). These resistive effects can be characterised by the conductivity, σ:

$$R = \frac{1}{\sigma}\frac{d}{A} \tag{2.17}$$

.

Secondly, there is also a capacitive current flow, due to immobile charge carriers, which are polarised. These capacitive effects are expressed by the dielectric constant (permittivity) ε:

$$C = \varepsilon\frac{A}{d} \tag{2.18}$$

In these equations d is the sample thickness, A the cross section. One has to state, that inductive effects are often negligible in electrochemical systems, so physically, a homogenous material is equivalent to a parallel connection of resistor R and capacitor C. Therefore, the impedance measured is given by:

$$Z = \frac{1}{\sum_i \frac{1}{Z_i}} = \frac{1}{\frac{1}{Z_R} + \frac{1}{Z_C}} = \frac{1}{\frac{1}{R}} + \frac{1}{\frac{1}{i\omega C}} = \frac{R}{1 + i\omega RC} \tag{2.19}$$

$$\lim_{\omega\to 0} \frac{R}{1 + i\omega RC} = R = Z_R \tag{2.20}$$

$$\lim_{\omega\to \infty} \frac{R}{1 + i\omega RC} = \frac{1}{i\omega C} = Z_C \tag{2.21}$$

Equation (2.19) suggests that at low frequencies the impedance of the capacitances are too high, so current flows rather through the resistances, while for high frequencies it is the other way round. This means, that between the low and high frequency regime the impedance is changing progressively from a resistance-type to a capacitance-type: the

impedance spectra of a homogenous material (ideal case) is a semicircle in the $-\mathrm{Im}(Z)$ vs. $\mathrm{Re}(Z)$ plot, whose important point is the characteristic frequency, given by:

$$f_{\mathrm{char}} = \frac{1}{2\pi RC} = \frac{1}{2\pi}\frac{\sigma}{\varepsilon} \tag{2.22}$$

For a polycrystalline material we have two semicircles, one for grains and the other for grain boundaries, as they differ in ε and particularly in σ. The diameter of the individual semicircles gives the resistance contributions, while from fitting also the capacitances can be evaluated.

These thoughts are only the basic ideas for electrochemical impedance spectroscopy, because a spectrum obtained from a more complex system is very complicated in most of the cases. Firstly, materials could have not only electronic, but also ionic conductivities, which despite of being not separately present in the spectra, can be evaluated. Furthermore, not only the bulk material properties contribute to the impedance spectra, but also the electrochemical processes proceeding through electrode reactions and charging of double layers and chemical capacitances. These contributions will be treated in Section 2.6. For the accurate evaluation of impedance spectra measured on electrochemically active polycrystalline materials, a model conception is needed which suggests a possible equivalent circuit, containing resisitive and capacitive elements. But if all results are well understood, EIS can quantify many crucial parameters of a system.

To sum up, electrochemical impedance spectroscopy has a very distinguished position in materials research and that is why it is the most important measurement method used in this work.

2.5 Electronic and ionic conductivity in solids

The electrical conduction in a solid consists of several contributions. Charged particles (electrons, holes and ions) can be transported across a solid under an externally applied

electric field. When several different charged species are rpesent and they all contribute to the conduction, the overall conductivity σ is simply the sum of the different contributions:

$$\sigma = \sum_i \sigma_i = \sigma_{\mathrm{e}'} + \sigma_{\mathrm{h}^\bullet} + \sum_{\text{ion.defects } j} \sigma_j \tag{2.23}$$

where

$$\sigma_i = zeu_i n_i \tag{2.24}$$

is the conductivity due to charged particle of type i, ze is the charge of the particle, u_i is the mobility and n_i its concentration.

The electronic conductivity is related to the type of the material. One can distinguish conductors (metals, some ceramic materials), semi-conductors (e.g. covalent and ionic ceramics) and insulators. In semi-conductors the concentration of mobile charged particles are determined by many factors: temperature (intrinsic electronic defects due to exciting electrons from the valence band to the conduction band, if $T > 0$ K), doping (generation of holes by adding acceptor dopants, or electrons due to donors), atmosphere. In this work, it is also investigated, how the electronic conductivity of ceria changes by variation of dopants and temperature. Furthermore, in the light of the above mentioned defect chemistry of ceria, the oxygen partial pressure is of crucial importance.

The ionic conductivity refers to the transport of ions (ionic defects, e.g. oxygen vacancies $\mathrm{V}_{\mathrm{O}}^{\bullet\bullet}$ in SOFC electrolytes and electrodes) across a solid, under an applied field. Section 2.1 describes the factors determining the concentration of ionic defects. It is very important, that temperature influences not only the concentration, but also the mobility of the charge carriers, which results in a thermally activated conductivity, characterised by an Arrhenius-type equation:

$$\sigma = \sigma_0 \exp\left(-\frac{E_{\mathrm{a}}}{kT}\right) \tag{2.25}$$

where E_{a} is the activation energy of the conductivity, and σ_0 is the pre-exponential factor. One can see immediately that the resistance being in relationship with the conductivity according to Equation (2.17) is also thermally activated, so the resistances obtained from

fitting of impedance spectra can be used instead of the conductivities to get and compare activation energies.

2.6 Use of EIS for investigating of reaction steps

Reaction kinetics

Why can the reaction kinetics be investigated by Electrochemical Impedance Spectroscopy? For the explanation, one should study the relationship between chemical kinetics and electrochemistry for a simple reaction:

$$\mathrm{A} + \mathrm{B} \rightleftharpoons \mathrm{C} \tag{2.26}$$

The reaction rate law expression connects the rate of a reaction to the concentrations of the reactants, as it can be seen in the following for a reaction of first order with respect to A and B:

$$r = \overrightarrow{k}\,[\mathrm{A}]\,[\mathrm{B}] - \overleftarrow{k}\,[\mathrm{C}] \tag{2.27}$$

where $\overrightarrow{k}$ and $\overleftarrow{k}$ are the rate constants of forward and backward reaction. A rate constant is thermally activated and thus follows the Arrhenius-law:

$$k = A \exp\left(-\frac{E_\mathrm{a}}{kT}\right) \tag{2.28}$$

In electrochemistry, the rate of reactions occuring on electrodes are usually expressed by current I (or current density j), given by:

$$I = zFr \tag{2.29}$$

where $F = 96485\ \dfrac{\mathrm{C}}{\mathrm{mol}}$ the Faraday-constant, z is the valence of the ions (charge number). For a small applied voltage, this current is proportional to the voltage. Therefore an electric (AC) resistance can be measured by EIS. Thus, the reaction rate of electrode processes can be investigated. However, electrode processes are very complicated in most cases, because

of the occurence of several reaction steps (sub-reactions). These are e.g. dissociative adsorption, followed by charge transfer and exchange between atmosphere and solid, from which the rate limiting step determines our measurement results (so the kinetics of the overall reaction). This step can not be identified in a simple way, usually only some basic facts can be established. We can say that one needs a high amount of precise measurements and consistent parameter variations to be able to develop an accurate reaction model.

Let us take the hydrogen oxidation reaction proceeding on the electrode, when molecular hydrogen forms water with oxygen anions, while two electrons are left behind:

$$H_2 + O^{2-} \rightleftharpoons H_2O + 2e^- \tag{2.30}$$

As it was said above, this is just the total reaction, being composed of several reaction steps. If we consider the three sub-reactions mentioned in the previous paragraph (adsorption, dissociation, oxidation), there are two different possible reaction paths for the overall reaction: the so called bulk path and the surface path [18].

In the surface path case (Figure 2.4 a)), molecular hydrogen coming from the atmosphere is adsorbed (and dissociates, as well) at the electrode surface. Then, the adsorbed hydrogen atom (maybe also partially ionised) diffuses along the surface until it reaches the triple phase boundary (gas phase-electrode-electrolyte), where the reaction with oxygen ions from the electrolyte occurs. This path is preferred, when the electrode material has no, or very low ionic conductivity.

The bulk (volume) path (Figure 2.4 b)) is possible for mixed ionic and electronic conductors, since the ionic conductivity makes it possible for oxygen ions to diffuse also through the electrode material. In this case, the whole electrode surface (electrode-gas interphase) is available for the reaction.

One has to mention, that it is not straightforward to distinguish between the two cases. This will be detailed in Section 5.6.

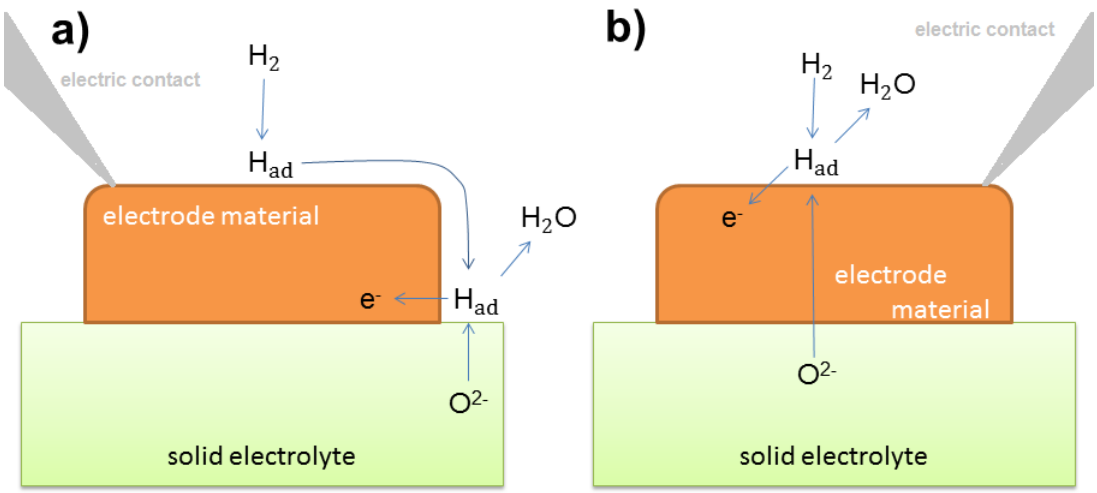

Figure 2.4: Possible reaction paths for the hydrogen oxidation, a) electrode surface path, b) electrode bulk path

Separation of electrode processes by means of EIS

When electronic and ionic charge transport in a material is fast, the oxygen exchange reaction is the rate-limiting step in the electric treatment. As it was mentioned above, in the electric treatment a finite reaction rate appears as a resistance. The current measured in EIS is proportional to the rate of conversion between electronic current in the electrode contact and ionic current in the electrolyte. When this conversion is also possible via a capacitive process (e.g. chemical capacitance, double-layer capacitance), an additional capacitor will appear in the circuit. Therefore, for electrode reactions we get semicircles in the impedance spectrum.

If the material has low electronic conductivity, other phenomena also should be taken into account, for instance, space charges (Schottky contacts) as resistances and capacitances.

Chapter 3

Experimental

3.1 Sample preparation

Targets of GDC and MnGDC (exact composition in Table 3.1) were preparated for PLD (pulsed laser deposition). GDC was a commercially available powder (*Treibacher Industrie AG, Austria*). MnGDC was sythesised from the mentioned GDC powder and $MnCO_3$ (99.9%, *Sigma-Aldrich Co.)* by shake and bake method. The powders were then cold isostatically pressed to pellets, and sintered at 1550°C for 2×5 hours. These materials were then analysed by X-ray diffraction in Bragg-Brentano geometry, with an X'Pert Powder PANalytical diffractometer, using β-filtered Cu-K_α radiation. The pellets served as targets for deposition after affixing them to a stainless steel target holder.

In Figure 3.1 and Figure 3.2 the XRD diffractograms of the target materials can be seen. The blue and green peaks are the measured peaks, while the red lines are references [19]. One can see, that GDC is pure, without any other phases, while MnGDC exhibits some small unidentified peaks present in the diffractogram. The thin films were deposited from these targets on one side polished yttria stabilised zirconia single crystals (YSZ, 9.5 mol% Y_2O_3 in ZrO_2, supplied by CrysTech GmbH Kristalltechnologie, Germany)

For a better electronic contact to the thin film, not only the electrode materials were

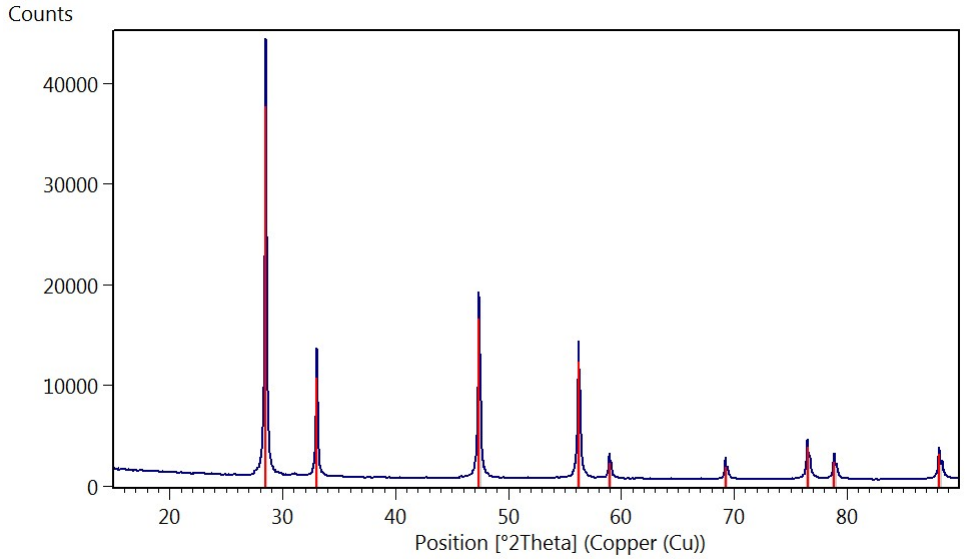

Figure 3.1: XRD diffractogram for GDC

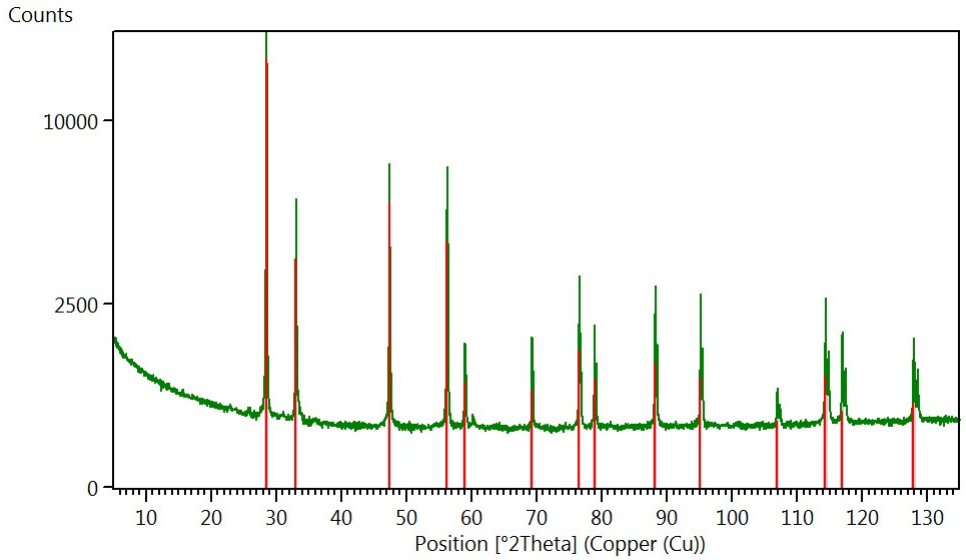

Figure 3.2: XRD diffractogram for MnGDC

deposited on the surface of the substrate but also metal grids (current collectors) from titanium (as an adhesive layer) and platinum were sputter-deposited beneath or on the top of the ceramic thin films. The current collectors have a specifically designed shape,

	Material	Composition
GDC	gadolinia doped ceria	$Gd_{0.2}Ce_{0.8}O_{1.9-\delta}$
MnGDC	manganese and gadolinia co-doped ceria	$Mn_{0.1}Gd_{0.18}Ce_{0.72}O_{1.9-\delta}$

Table 3.1: Prepared thin films: materials and their composition

which is described in Section 3.5.

Dimensions of the substrate: 10 mm×10 mm×0.5 mm for samples with microelectrodes (micro samples), 5 mm × 5 mm × 0.5 mm for samples with only macroscopically sized electrodes (macro samples). To study the influence of the crystallographic orientation on the electrochemical properties, two types of one side-polished yttria stabilized zirconia single crystals, (100)-oriented (polished parallel to the (100)-plane) and (111)-oriented, were used as substrates for the thin films.

The schematic flowchart (Figure 3.3) shows the preparation steps of the working electrode for samples with metal grids beneath or on top of the electrode for macro samples and for micro samples. As it can be seen, the preparation of macro samples is not as critical as it is for micro samples, because in this case the electrodes are not micro-stuctured. The macro samples had LSF ($LaSr_{0.6}Fe_{0.4}O_3$)-Pt two layer counter eletrodes on the non-polished side of the YSZ-substrate, whose preparation preceded the first step of manufacturing our working electrode (anode): at first, LSF-paste with ethylcellulose as pore-former (solvent: terpineol) was spread on the non-polished side of the YSZ and was dried at 100 °C. Then, Pt-paste was brushed on the sample and finally, the sample was sintered at 850 °C for 5 hours. The temperature programme for the sintering can be seen in the Figure 3.4.

In the following sections the preparation steps of the working electrodes will be discussed in details.

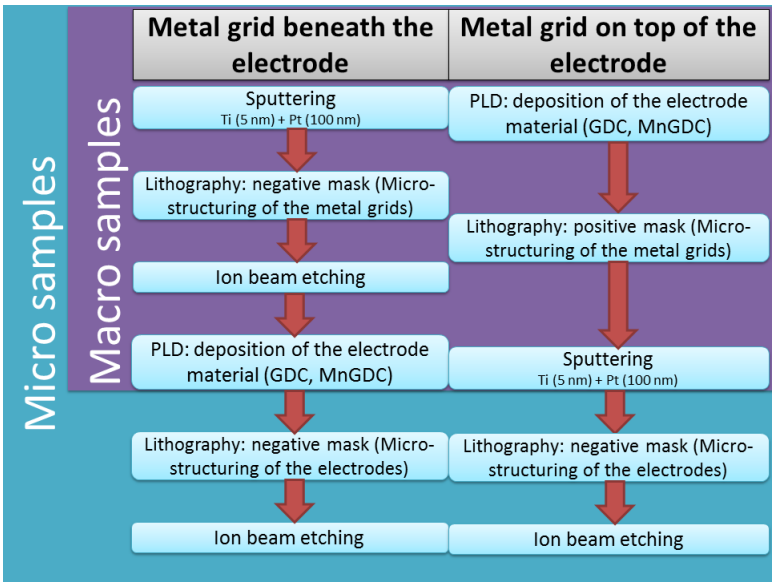

Figure 3.3: Preparation steps of the working electrode for samples with metal grids beneath or on top of the electrode for macro samples and for micro samples

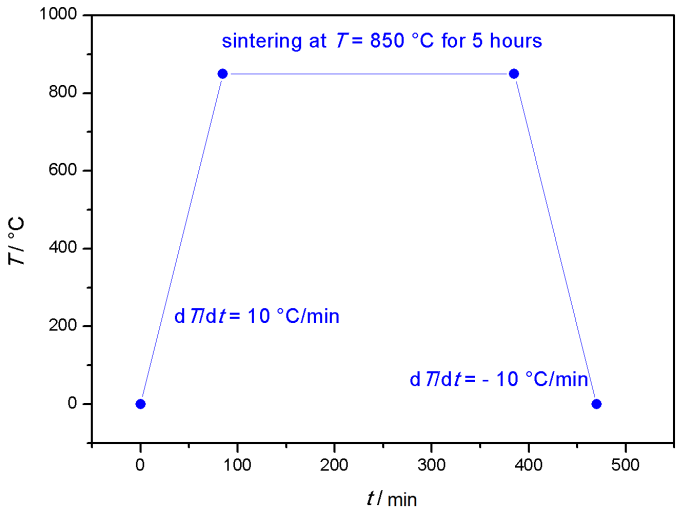

Figure 3.4: Temperature programme for sintering of the reference electrode

3.2 Sputtering

For the purpose of better electronic conductivity compared to the MIEC layer, titanium and platinum layers serving were deposited on the surface of the substrate by cathode sputtering in a firstly to $\sim 10^{-5}$ mbar evacuated and then by argon filled sputtering machine (MCS 020, BAL-TEC AG, Germany), Figure 3.5. The parameters for sputtering are shown in Table 3.2. As the thickness of the metal layer can be varied by means of the sputtering time, it was calculated from a known deposition rate, which is $0,18\ \mathrm{nm \cdot s^{-1}}$ for Ti and $0,8\ \mathrm{nm \cdot s^{-1}}$ for Pt. As it was mentioned above, titanium serves only as an adhesion promoter, so it was made much thinner than platinum.

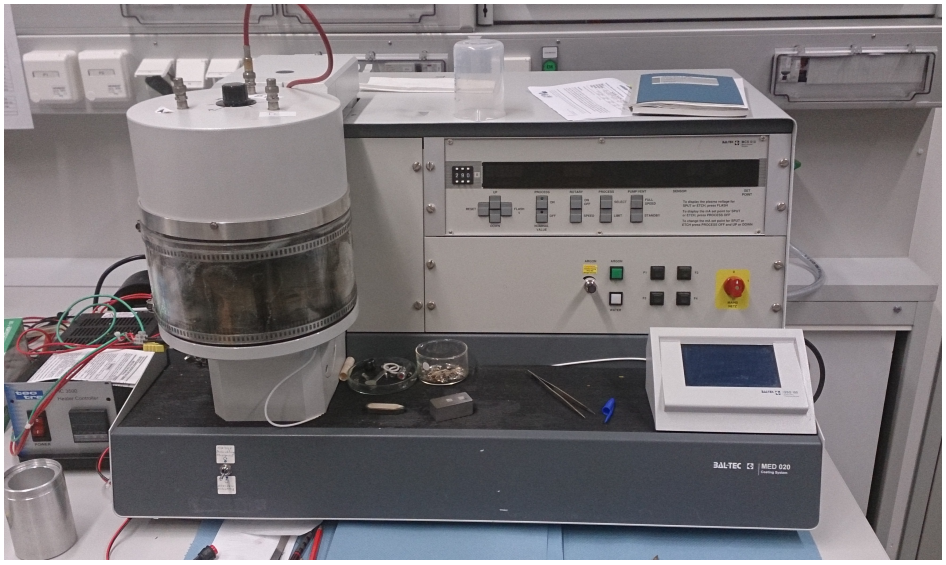

Figure 3.5: Sputtering machine

Metal	Thickness / nm	Dep. time / s	p_{Ar} / mbar	Current I / mA
Ti	5	28	$7 \cdot 10^{-3}$	100
Pt	100	125	$2 \cdot 10^{-2}$	100

Table 3.2: Parameters of sputtering

3.3 Lithography

Since the metal grids and in the case of the micro samples also the electrodes had to be micro-structured, ion beam etching and lift-off lithographic techniques were applied. At first, the sample was covered with 100 μl photoresist and spin-coated at 50 rpm for 30 seconds in order to achieve a thin layer of the photoresist on its top. After drying at 100 °C for 2 minutes, the photoresist was exposured to UV-light through a photomask (Figure 3.6, Figure 3.7) using several different patterns (fingers for structuring of the metal grids, rectangle shape for the electrodes, Figure **??**). Thus the hardening of the photoresist occured where it was not covered by the mask. The non-hardened photoresist in the covered areas could be removed by dissolving in an alkaline developer solution.

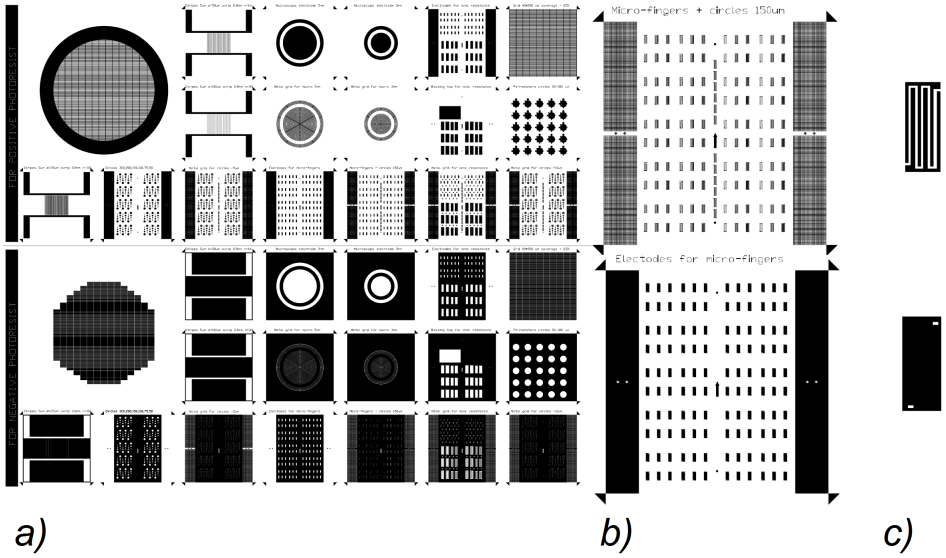

Figure 3.6: a) Scheme of the photolithographic mask used for preparing micro samples, with b) the finger design for the metal grids, and the rectangles for the electrode material, c) the individual microelectrodes. The exact geometry of the metal fingers will be discussed in the following.

The lithographic technique and thus the mask to be used (positive or negative) are different, depending on how the structuring is carried out after the lithographic step.

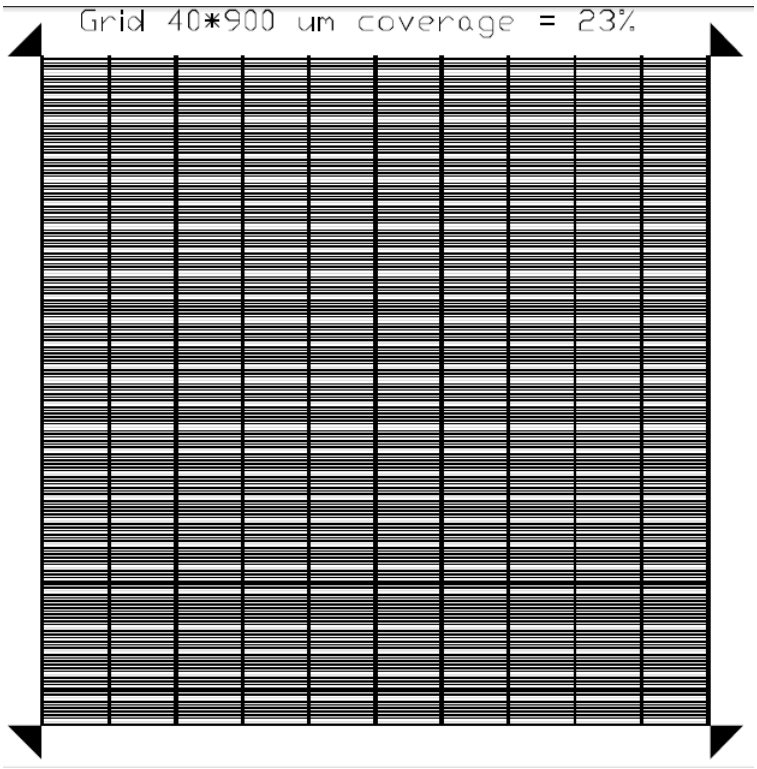

Figure 3.7: Drawing of the photolithographic mask used for preparing macro samples.

1. *Standard lithography (Ion beam etching)*

   For structures of the metal or the electrode material being manufactured by ion beam etching, the mask for negative photoresist was used. This means, unwanted areas of the layer were covered by the mask. These were uncovered after developing and therefore removed in the following ion beam etching step and areas with still present hardened photoresist on the top remain.

   For removing the unwanted areas, the sample with the patterned photoresist on the top was placed in a vacuum chamber (evacuated to $\sim 10^{-5}$ mbar) and exposed to a focused argon ion beam (plasma at about 10^{-4} mbar). As mentioned in Section 3.3, if the structure was manufactured by ion beam etching, the result of the lithography had been a pattern left behind in the photoresist and that some areas of the thin films or metal layer had been masked from the exposure of the etching beam: the

impact of the ions erodes the material, abrading away areas not protected by the hardened photoresist. After the process the sample was taken out and put into pure ethyl-alcohol.

2. *Lift-off lithography*

   The samples with the metal fingers on top of the electrode were preparated by using lift-off lithography. The basic idea of it is to remove the metal from regions by dissolving previously spread photoresist beneath the metal. Thin film regions that should remain, were covered by the mask (mask for positive photoresist). After the UV-exposition step, the not hardened photoresist (over regions where electrodes should be) was removed. The sample was then covered by sputter-deposited Ti and Pt and subsequently put into ethanol p.A. Therefore the electrodes were lifted off by dissolution of the still present photoresist, leaving behind the metal fingers.

Illustrations for the lithographic techniques mentioned can be found among others in [20].

3.4 Pulsed laser deposition

The electrode material (GDC or MnGDC) was ablated by a high-power pulsed laser beam (KrF excimer-laser, Lambda COMPexPro 201F, $\lambda = 248$ nm) from the surface of a target fixed on a rotating stainless steel target holder. To avoid contaminations on the surface, the chamber was firstly evacuated to $\sim 10^{-5}$ mbar pressure with a turbomolecular pump. While rotating, the material was deposited in a pure oxygen atmosphere at $4 \cdot 10^{-2}$ mbar oxygen partial pressure and at $\sim$ 650 °C substrate temperature. The temperature was controlled by a pyrometer. According to the experiences of depositions carried out earlier, the deposition rate was $\sim$ 13.3 nmmin^{-1} for both materials. In most of the cases the deposition time was chosen so that a film thickness of 200 nm resulted, but samples for

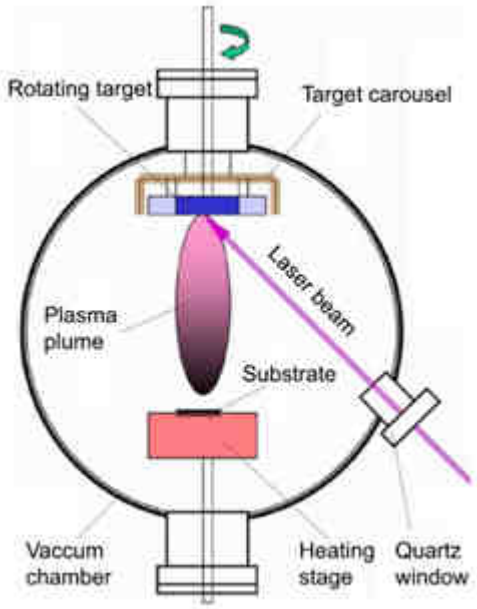

Figure 3.8: Scheme of the PLD device [3]

SIMS measurements were prepared also with thinner or thicker films. The energy of the laser pulse was 400 mJ and the pulse repetition rate (frequency) 5 Hz. The scheme of the PLD device can be seen in Figure 3.8.

3.5 Microelectrodes, electrode shape

The microelectrode samples consisted of several microelectrodes and two large counter electrodes (see Figure 3.6 b)). The mask used for the lithographic patterning of the metal grids contained three different finger shapes, which differ in the number of the fingers. This means, that the finger distance is different. A part of a micro sample with the electrodes and the mentioned three different metal finger shapes can be seen in Figure 3.9. The exact measures of each current collector shape are given in Table 3.3.

One can see, that the finger structure consists of separate metal combs. This has the big advantage for the impedance measurements, that the combs can be contacted either

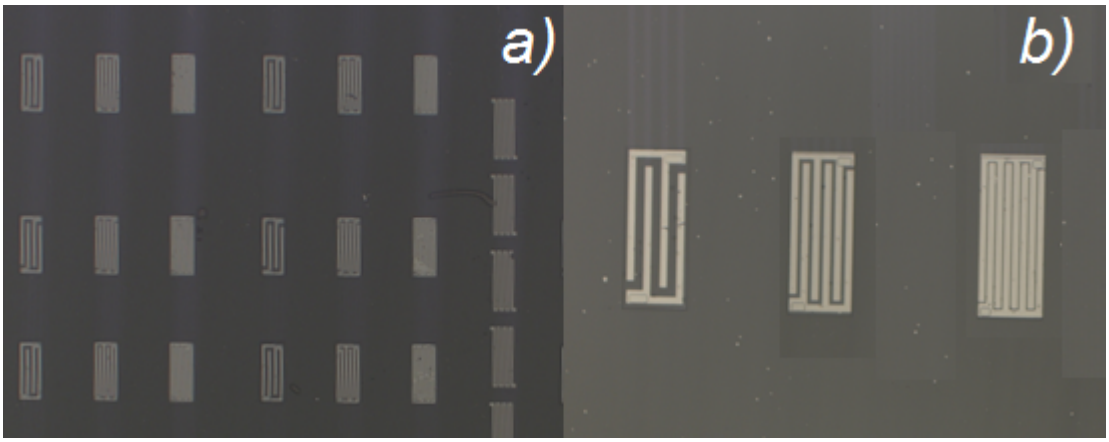

Figure 3.9: Microelectrode sample with buried metal fingers a) part of the sample, b) the three different metal fingers

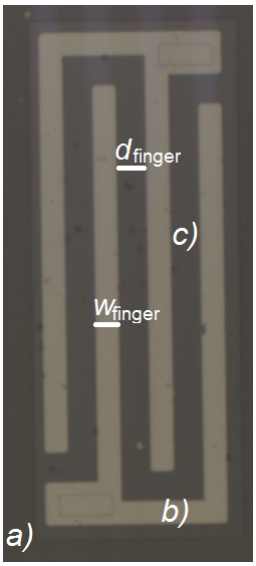

Figure 3.10: Microelectrode with buried metal grid *a)* YSZ-substrate; *b)* Ti/Pt (5 nm/100 nm) layer, metal fingers beneath the electrode; *c)* rectangular MIEC electrode (GDC or MnGDC), 200 nm thin film; w_{finger}: finger width, d_{finger}: finger distance. The electrode border is highlighted by a black line.

Name	number of fingers	finger width - w_{finger}/μm	finger distance - d_{finger}/μm
finger big	4	15	25
finger middle	6	15	11.7
finger small	8	15	5

Table 3.3: Measures of the three different metal finger shapes

in series (in-plane mode, Figure 3.11), or in a parallel connection (out-of-plane mode, electrochemical mode, Figure 3.12). In this way, the contributions from different processes can be separated from each other.

- *In-plane mode*

  The separate combs have opposite potential, as the voltage is applied between them. One of the metal fingers is cathodic, the other is anodically polarised (of course alternately because of the alternating current), leading to the reactions Equation (3.1), Equation (3.2). Additionally, also an electronic current can flow between the metal fingers, which makes the investigation of the electronic conduction within the thin film possible (which also occurs without any electrochemical reactions).

$$\text{K(-):} \qquad H_2O + V_O^{\bullet\bullet} + 2e' \longrightarrow O_O^{\times} + H_2 \tag{3.1}$$

$$\text{A(+):} \qquad O_O^{\times} + H_2 \longrightarrow H_2O + V_O^{\bullet\bullet} + 2e' \tag{3.2}$$

- *Electrochemical mode*

  The metal fingers are on the same potential and the voltage is applied between the microelectrode and a macroscopic counter electrode which is also on the sample (see Figure 3.6 b) on the edges). This measurement mode is usually employed for impedance studies on microelectrodes and is sensitive on the oxygen exchange activity. The advantage of measuring the small working electrodes against an extended counter

electrode is that because of the large area ratio (1 : 300) the resistance of the counter electrode can be neglected.

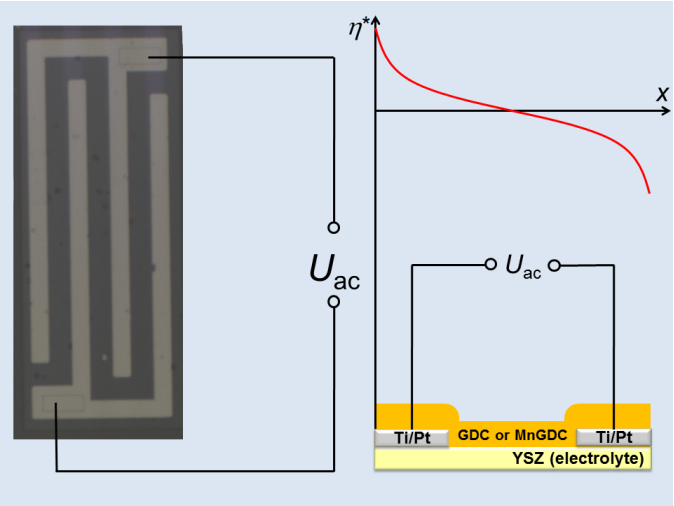

Figure 3.11: Sketch of the in-plane measurement (η^*: polarisation potential, see Section 4.1)

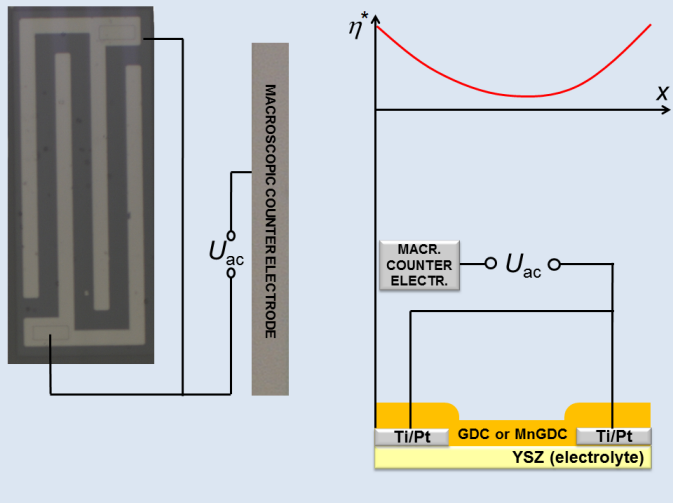

Figure 3.12: Sketch of the electrochemical measurement (η^*: polarisation potential, see Section 4.1)

3.6 Electrochemical impedance spectroscopy

The characterisation of the electrode materials were carried out by a *Novocontrol Alpha-A High Performance Frequency Analyser*, with a *Novocontrol POT/GAL 30V/2A interface*. Using this system, direct current and direct current-polarised impedance measurements can be performed.

The impedance spectra were acquired in two different setups. Both measurement devices make it possible to have a defined gas atmosphere that can be applied during the measurement, and since they act as Faraday cages, they help to avoid measurement artifacts caused by electrical noise and temperature changes. These devices were filled with humidified 2.5% H_2 containing Ar carrier gas. In this atmosphere the measurements were carried out in the (set) temperature range between 400 °C and 700 °C. Parameters: 0.01 V voltage (RMS), 10^6 Hz – 10^{-2} Hz frequency range. In some cases also bias voltage was used.

Macro measurements

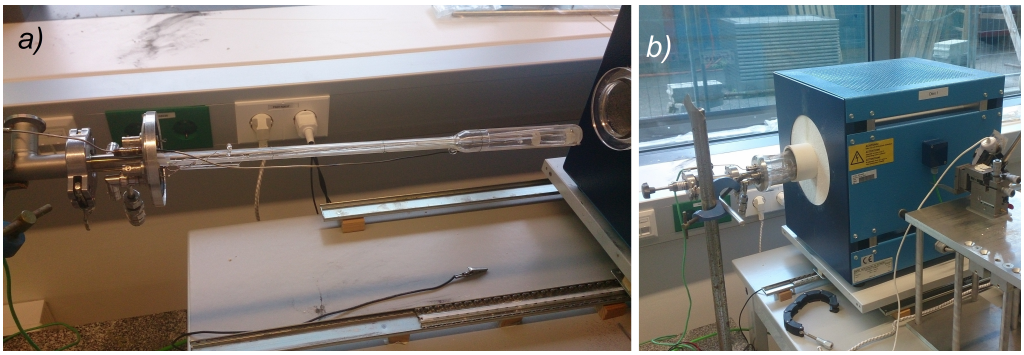

Figure 3.13: Impedance measurement station for macro samples a) the quartz tube with the Pt wires and the thermocouple, b) the furnace

Macro samples were measured in macro devices (a shielded quartz tube), see Figure 3.13. The samples were contacted by two platinum sheets, one in contact with the whole surface

of the macro electrode, the other with the LSF counter electrode. The quartz tubes with the samples were heated in a tube, the temperature of which was controlled by a *Eurotherm 3200* controller and the exact temperature was measured by a thermocouple placed near to the sample.

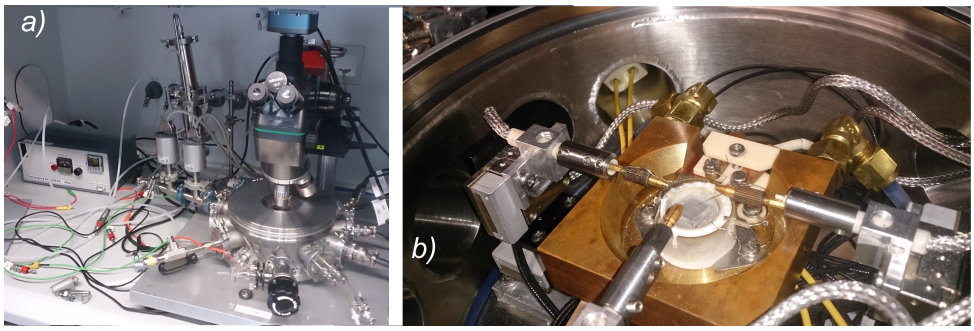

Figure 3.14: Impedance measurement station for micro samples a) the closed chamber, microscope, gas washing device and the heater b) the heating stage with sample and needles

For micro samples, a micro-contact measurement station was applied, which is a sealed stainless steel chamber (Figure 3.14). In case of micro samples gold plated steel needles were used for contacting the electrodes. They have sufficiently sharp tips and make a reliable electrode contact possible, but the limited stability of the gold plating at higher temperatures had to be paid attention to, as this may cause a contact resistance. The needles could be moved by high-precision linear piezoelectric stages (*Newport Agilis*), which were controlled by a computer interface. To be able to contact the microelectrodes, a microscope was used for accurate observation of the sample.

The micro samples were placed on a heating stage which was heated by a *Linkam TS1000 EV 17/3* heater. To be able to analyse the measurement results, it is also very important to know the exact temperature, also in the case of micro samples. However, it is always different from the set temperature of the heater. For instance, because of the position of the sample on the heating stage, the heater temperature is always higher than

the actual microelectrode temperature. So, a measurement method had to be found, which is capable of providing an (approximately) exact surface temperature (T_{real}). For this, the YSZ spreading resistance offers a good opportunity. It is caused by the ohmic resistance of the electrolyte and can be measured by impedance spectroscopy (often visible as a high frequency intercept in the measured spectrum) [9]. Based on the spreading resistance formula for circular electrodes (Equation (3.3)), the temperature can be calculated also for rectangular electrodes by an appropriate equation, if the temperature dependence of the YSZ resistance is known [21]. If the thickness of the sample is much bigger than the diameter of a circular the microelectrode, the ohmic drop is given by [9]:

$$R_{\mathrm{YSZ}} = \frac{1}{2\sigma_{\mathrm{ion,YSZ}} d_{\mathrm{me}}} \tag{3.3}$$

where $\sigma_{\mathrm{ion,YSZ}}$ is the ionic conductivity of YSZ, d_{me} is the diameter of the microelectrode. The spreading resistance of the rectangular electrodes used here was found to be equal to that of 300 μm circular electrodes.

Chapter 4

Equivalent circiut model for ceria-based anodes

The new electrode and metal grid design (developed by Andreas Nenning, [22]) makes it possible to separate the effects contributing to the polarisation resistance and to quantify them by EIS measurements. According to [22], the experimentally measured spectra can be fitted by the use of an electrochemically motivated and thoroughly deduced equivalent circuit model.

4.1 Electrode geometry and current paths

The thickness of the MIEC electrode layer on YSZ is 200 nm in the case of the samples manufactured in the present work. This means, that the electrodes are very flat, while for microelectrodes, the smallest lateral feature is 5 μm, which is wide in comparison to the film thickness, so the surface-thickness ratio is relatively high.

Due to this high aspect ratio, current will be treated differently in the lateral and the vertical direction. According to the equation $R = \varrho\frac{\ell}{A}$, which expresses the resistance of a

conductor of uniform cross section A and length ℓ, one can write:

$$R_{\text{lateral}} \sim \frac{\ell}{d} \tag{4.1}$$

and

$$R_{\text{vertical}} \sim \frac{d}{\ell} \tag{4.2}$$

where d is the film thickness, ℓ is the lateral feature size (finger distance). The two resistances in comparison:

$$\frac{R_{\text{lateral}}}{R_{\text{vertical}}} \sim \frac{\ell^2}{d^2} \tag{4.3}$$

Being ca. 600 times smaller in the case of the present work, the vertical resistance can be neglected, while the lateral resistance has a high influence on the impedance spectra.

In regions of the sample, where the electrode material and the metal finger are in direct contact, the electron conduction takes place in the current collector. One can write: $\nabla\tilde{\mu}_{\text{e}^-} = 0$, where $\tilde{\mu}_{\text{e}^-}$ is the electrochemical potential of electrons. As the electronic resistance can be neglected, the charge transport resistance is caused by the lateral ionic transport. In addition to this loss, also the electrochemical reaction (oxygen incorporation and release) has to be taken into account, because of its finite rate, which is electrically treated as an area specific surface resistance, which is a feature of oxygen exchange activity.

As the electrode material is a poor electronic conductor, in the regions without metal finger the electronic charge transport losses are relevant beside the resistance caused by the electrochemical surface reaction. Because of the electric contact with the YSZ, which is a good ionic conductor, $\nabla\tilde{\mu}_{\text{O}^{2-}} = 0$ can be assumed.

In the two areas mentioned above, the polarisation depends on the ratio of the lateral (ionic or electronic) resistance and the surface resistance. In a certain distance from the triple phase boundary (from the edge of the metal grid) polarisation converges to zero. For this distance, one can define a measure, the so called characteristic length, κ (Equation (4.7) which is the distance where the polarisation potential η^* drops to $\frac{1}{e}$ on an electrode with metal finger distance $d \gg \kappa$.

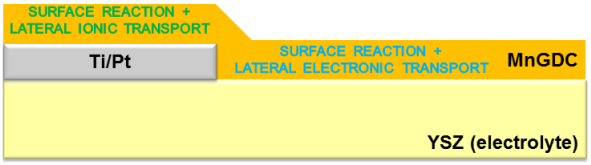

Figure 4.1: Effects causing the polarisation resistance of the electrode in different regions

$$\eta^*(x = \kappa) = \frac{1}{e}\eta^*(x = 0) \tag{4.4}$$

The polarisation potential η^* is a local measure for the driving force of oxygen exchange. This measure can be connected to the local difference in the chemical potential of oxygen ions between the electrode and the atmosphere, which acts as the driving force for oxygen exchange, as it can be seen in Equation (4.5).

$$\eta^*(x) = \frac{\Delta\tilde{\mu}^{\text{electrode}}_{O^{2-}}}{2F} \tag{4.5}$$

if the surface reaction is rate-limiting (compared to the across plane charge transport and interfacial charge transfer at Ti/Pt/YSZ and MIEC/YSZ), Δ indicates the deviation from equlibrium. At the current collector borders ($x = 0$), we find:

$$\eta^*(x = 0) = U \tag{4.6}$$

With these assumptions, and by the use of Equation (4.6) and Equation (4.5), according to [22], the characteristic length can be calculated by means of Equation (4.7).

$$\kappa = \sqrt{\frac{R_{\text{surface}}}{R_{\text{lateral}}}} \tag{4.7}$$

The calculation is visualised in Figure 4.2.

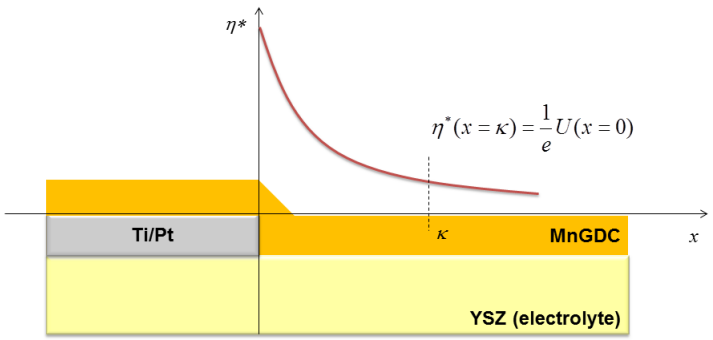

Figure 4.2: Polarisation in different regions of an electrode with large metal finger distance, definiton of the characteristic length κ.

4.2 Descriptive interpretation

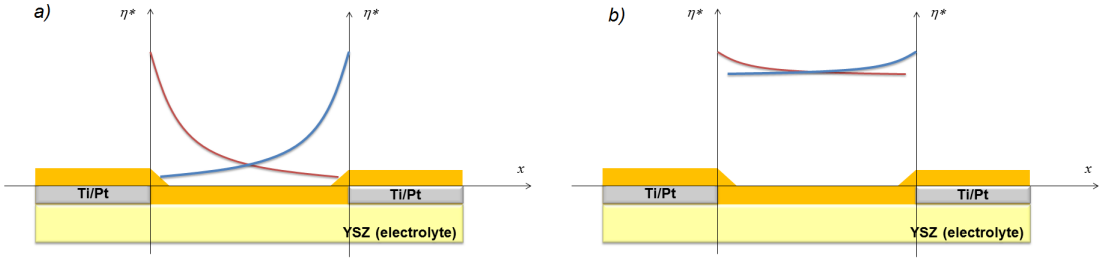

Figure 4.3: Interference of polarisations between two metal fingers a) for low electronic conduction, characteristic length is small; b) higher electronic conductivity leads to larger characteristic length and homogenous polarisation

As it was mentioned above, the polarisation decreases exponentially with distance. In our electrochemical measurements, where all metal fingers are anodically polarised (and are on the same potential), this means that the two exponential polarisation functions overlap between two metal fingers, resembling a hyperbolic cosine function, that describes the polarisation distribution in the mentioned area. As it can be seen in Figure 4.3, if the exponential functions are steep, the characteristic length is small, therefore regions in the middle of the free electrode surface are almost not polarised ($\kappa \ll d$). On the other hand,

for flatter functions (larger κ) the whole area between the metal grids can be polarised ($\kappa > d$). Therefore, a GDC electrode with small finger distance exhibits (approximately) homogenous polarisation in the electrochemical mode, while for bigger distances the same electrode material not the entire region between the metal grids is polarised.

At this point, it has to be noted, that the meaning of big and small finger distances, or flatter and steeper functions is depending on the oxygen incorporation activity and the lateral electronic conductivity. If the sample (e.g. fresh, non-degraded surface) exhibits very good oxygen exchange activity, also the smallest finger distance (5 μm) can be larger than κ and high electronic conductivity or low surface activity may lead to homogenous polarisation even for the biggest distance.

A good oxygen incorporation activity means, that electrons will be consumed already in the region very near to the triple phase boundary. This is the reason why the mechanistic interpretation of a surface resistance dependening on the geometry is not trivial: triple and two phase boundary activity cannot be undoubtedly separated, because an activity scaling with the triple phase boundary length may actually be a two phase boundary activity with a small characteristic length. For this reason, the triple phase boundary activity should be treated carefully in the following.

4.3 Equivalent circuit, model conception

The measured spectra contain all important information we want to know about our electrochemical system. In order to be able to get access to this detailed information, we need a model, which takes into account all processes that may influence the impedance spectra and which can be converted into an equivalent circuit. This means, each elementary process is translated into an equivalent circuit element. The relevant reactions and charge transport paths that were discussed in the previous sections will now be translated into an equivalent circuit model.

This way, the in-plane and electrochemical measurements can be fitted, and thr electronic and the ionic conductivity as well as the area specific resistance of the surface reaction and chemical capacitance can be quantified.

In the following, the main thoughts of the equivalent circuit model by Andreas Nenning will be treated. In details it can be read in [22]. With metal combs beneath the electrode, the whole electrode area is in exchange with the gas atmosphere, the whole surface can be electrochemically active (can exchange oxygen), but it depends on the material properties (ionic and electronic conductivity in the different regions), how much of it is really active.

- *Region above the YSZ substrate*

  In this region, electronic transport losses and losses caused by the surface reaction have to be taken into account. It was modelled by a transmission line with a short circuit in the ionic rail ($\nabla\tilde{\mu}_{O^{2-}} = 0$), the electronic sheet resistance was treated in the electronic rail. Electrochemical reactions were treated with a simple $R \parallel C$ element, consisting of the area specific resistance of the surface reaction and chemical capacitance. Resistive contributions of the GDC-YSZ and MnGDC/YSZ interface were too small to be consistently fitted.

- *Region above the metal grid*

  In this region electronic transport losses can be neglected, as electronic transport occurs in the metal which is a very good electronic conductor. Ionic transport losses caused by O^{2-} transport in the electrode material should be considered, however, which is modelled by an additional transmission line with lossless electronic and resistive ionic transport. For the electrochemical reaction we need an $R \parallel C$ element, consisting of redox-resistance and chemical capacitance. In the system, also an YSZ-Pt interface is present, which appears in the equivalent circiut as a double-layer capacitance.

The thoughts mentioned above are visualised in Figure 4.4.

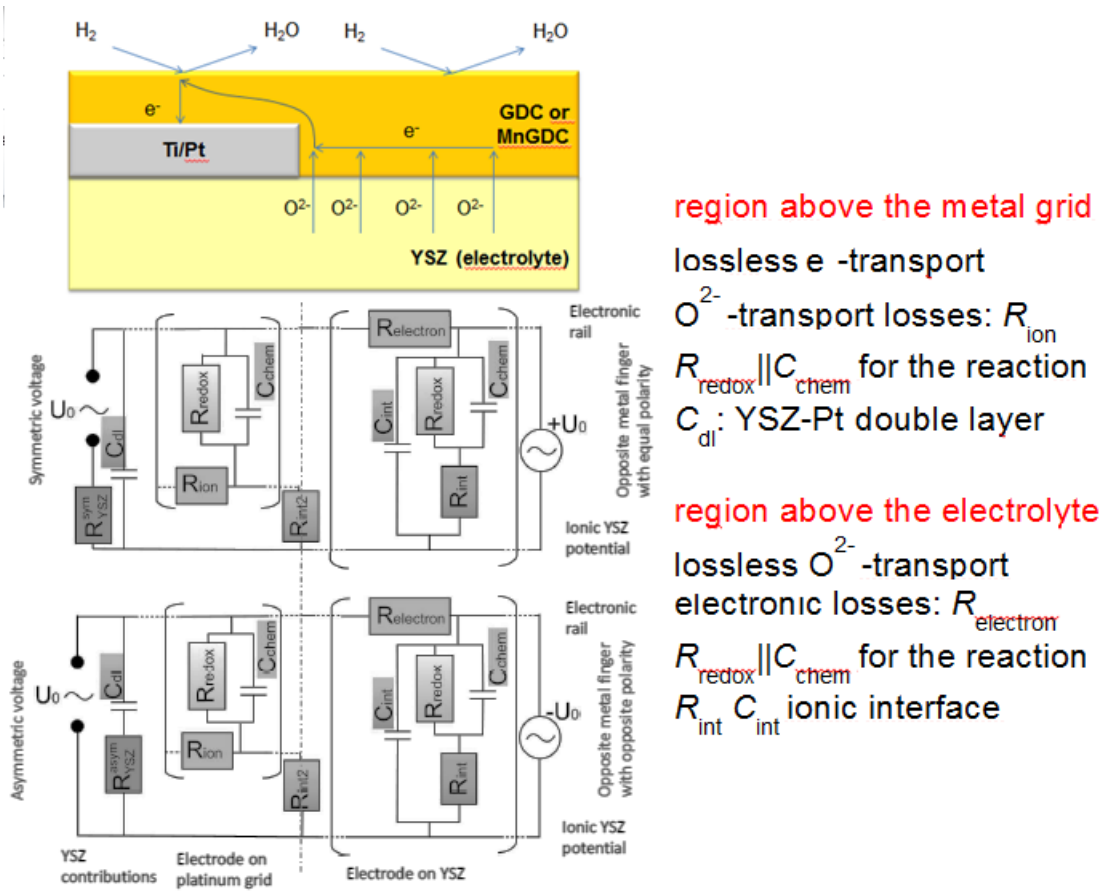

Figure 4.4: Equivalent circuit used for fitting of spectra obtained by measuring of micro samples with buried current collectors (based on [22]). R_{redox} corresponds to R_{surface} in this work.

Examples for the fitting will be sketched in Section 5.1 in Figure 5.3. This shows, that our model conception is suitable for fitting.

Measurements on macroscopic samples were fitted using a strongly simplified circuit (Figure 4.5) which is interpreted by assuming nearly homogenous polarisation and rate-limiting suface kinetics. Instead of an ideal capacitance a constant phase element (CPE) was used:

$$Z_{\text{CPE}} = \frac{1}{T(i\omega)^P} \tag{4.8}$$

and capacitances were calculated using:

$$C = \left(R_2^{1-P}T\right)^{\frac{1}{P}} \tag{4.9}$$

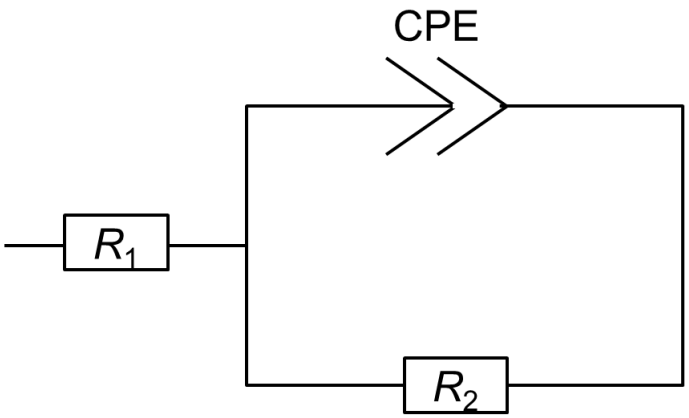

Figure 4.5: Equivalent circuit for fitting of the macro spectra.

Chapter 5

Results and discussion

5.1 Measured spectra, interpretation

In this part, examples of spectra are presented for different finger distances and measurement modes. At first, two observations have to be mentioned. Firstly, the two investigated materials (GDC and MnGDC) exhibit no significant difference in respect of the form of the impedance spectra and in electrochemical behaviour. Secondly, samples with current collectors on top of the electrode material show better catalytic activity in all cases when the resistance is normalised to the atmosphere-exposed surface: the Pt also seems to exhibit a significant catalytic activity for the oxygen exchange reaction. (This phenomenon will be demonstrated in Section 5.2 when the macro measurements are discussed.) For this reason, the characterisation of the electrode materials (evaluation of material parameters) was carried out on the basis of the results obtained by measuring samples with buried current collectors. In spite of this osbervation, the study of samples with metal grid on top is interesting and was also performed in this work, but for other reasons, e.g. for the investigation of reaction paths.

Figure 5.1 shows two typical spectra (in-plane and electrochemical) for the materials and Figure 5.2 displays the dependence of the shape of the impedance spectra on the finger

distance. For the in-plane measurements the size of the semicircle changes: the bigger the finger distance, the bigger the semicircle, which is not surprising, as for bigger finger distances the transport length of electrons is longer, the electronic resistance is higher.

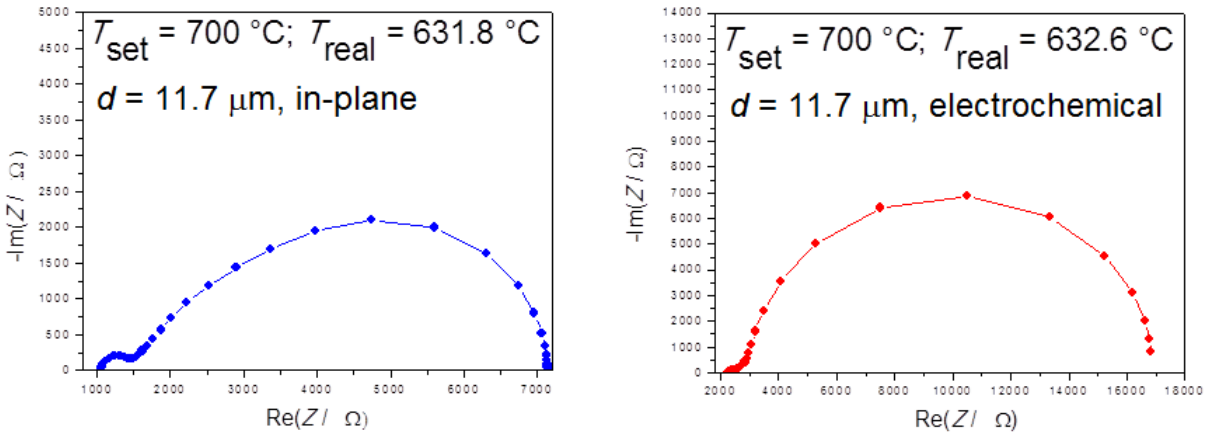

Figure 5.1: Examples for measured in-plane and electrochemical spectra of a microelectrode (MnGDC micro sample, metal grid beneath the electrode material, set temperature 700 °C); d: finger distance.

An important conclusion can be drawn from the electrochemical semicircles: as it can be seen in Figure 5.2, they have more or less the same size for all finger distances, it makes no difference, how many fingers we have beneath the electrode material. This suggests, that the whole surface area is electrochemically active for the three investigated geometry. Electrons can flow also between the fingers in the MIEC electrode, they can be transported all over these areas. This result was used for the construction of the equivalent circuit model: electronic and ionic transport in the electrode material could be fitted, but plays only a minor role in the electrochemical DC-resistance.

The model used for a simultaneous fit of two spectra measured on one microelectrode was already mentioned in Section 4.3 (transmission lines in Figure 4.4). Figure 5.3 shows examples for fitting of in-plane and electrochemical measurements and illustrates the appro-

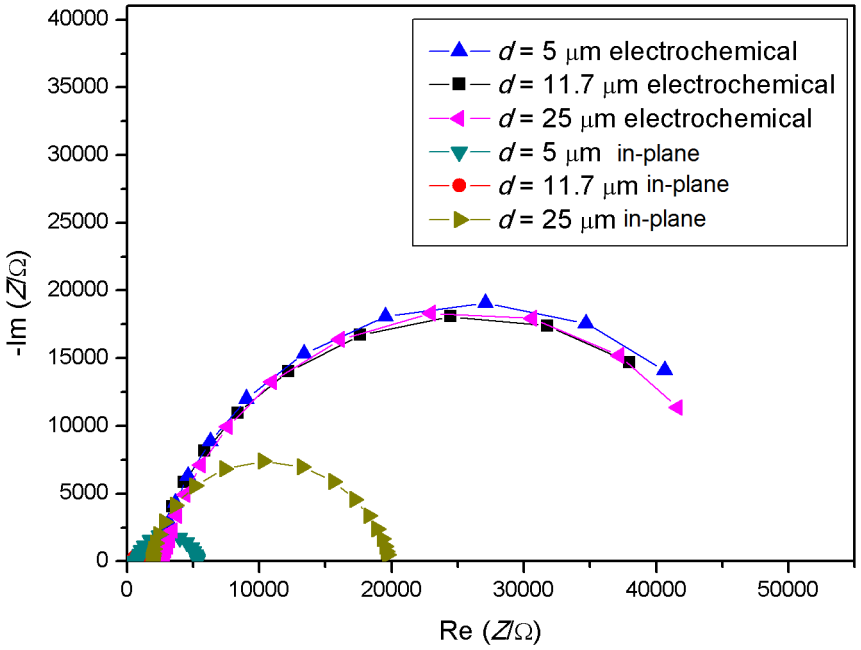

Figure 5.2: Finger distance dependence of the spectra - (MnGDC micro sample, metal grid beneath the electrode material, set temperature 700 °C); d: finger distance.

priateness of this model. The successful fitting of these spectra makes it possible to determine several properties (fit parameters): electronic sheet resistance ($R_{\text{electronic}} = \frac{1}{\sigma_{\text{electronic}} d}$), ionic sheet resistance ($R_{\text{ionic}} = \frac{1}{\sigma_{\text{ionic}} d}$), area specific surface resistance (R_{surface}) and chemical capacitance ($C_{\text{chem, fit}}$). In this way, the volume specific chemical capacitance:

$$C_{\text{chem}} = C_{\text{chem, fit}} \cdot \frac{1}{d} \tag{5.1}$$

where $C_{\text{chem, fit}}$ is the chemical capacitance provided by the fit model and d is the film thickness.

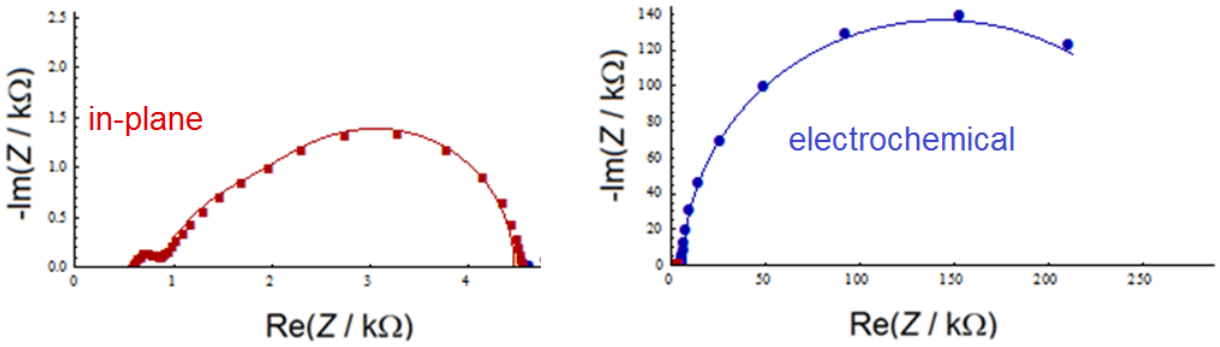

Figure 5.3: Examples for fitting (MnGDC micro sample, 11.7 μm finger distance, buried current collectors, $T_{\text{set}} = 700$ °C).

5.2 Temperature dependence, activation energies, degradation effects

In order to investigate the activation energy of different processes taking place in the materials, EIS measurements were carried out at different temperatures, between 400 °C and 700 °C set temperatures, step by step, with successively increasing temperatures. Then, the reverse direction (decreasing temperature) was measured as well, to see whether there are irreversible changes in the behaviour of the material due to the increased temperature.

Impedance spectra measured on *micro samples* at different temperatures (examples are shown in Figure 5.4, Figure 5.5) were again fitted by the model mentioned in Section 4.3 and the activation energies of the different electrochemical processes were calculated after plotting their characteristic quantities in Arrhenius plots. T_{real} was determined from the high frequency intercept resistance.

Fitting results from *macro measurements* were also evaluated in Arrhenius plots. As for macro samples degradation does not occur so fast, more temperature cycles could be carried out, providing a better evaluation of activation energies due to the high number of measured points.

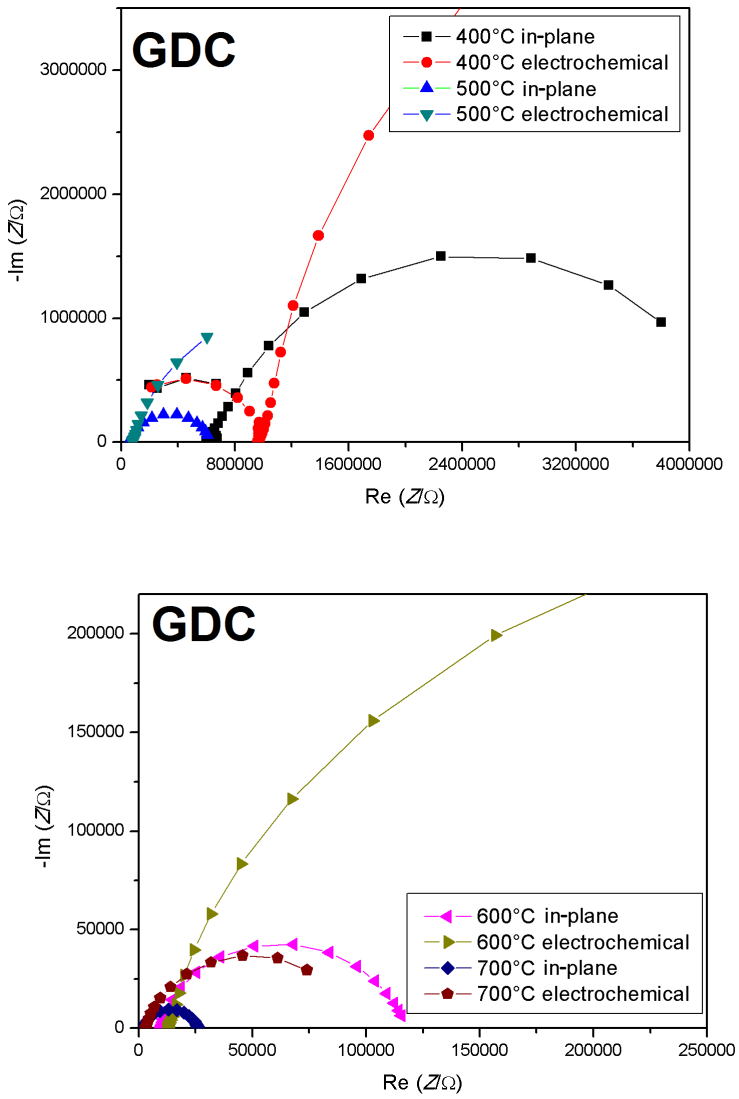

Figure 5.4: Temperature dependence of the spectra - measured EIS spectra at different set temperatures (GDC micro sample, 11.7 μm finger distance, buried current collectors).

Micro samples

For better investigation of degradation processes occuring on the sample, the impedance spectra in the cooling direction (temperature down) were taken only after measuring at the highest temperature for a longer time. In this way, degradation processes could be observed in real time. In Figure 5.6 Arrhenius plots for electronic and ionic resistances are

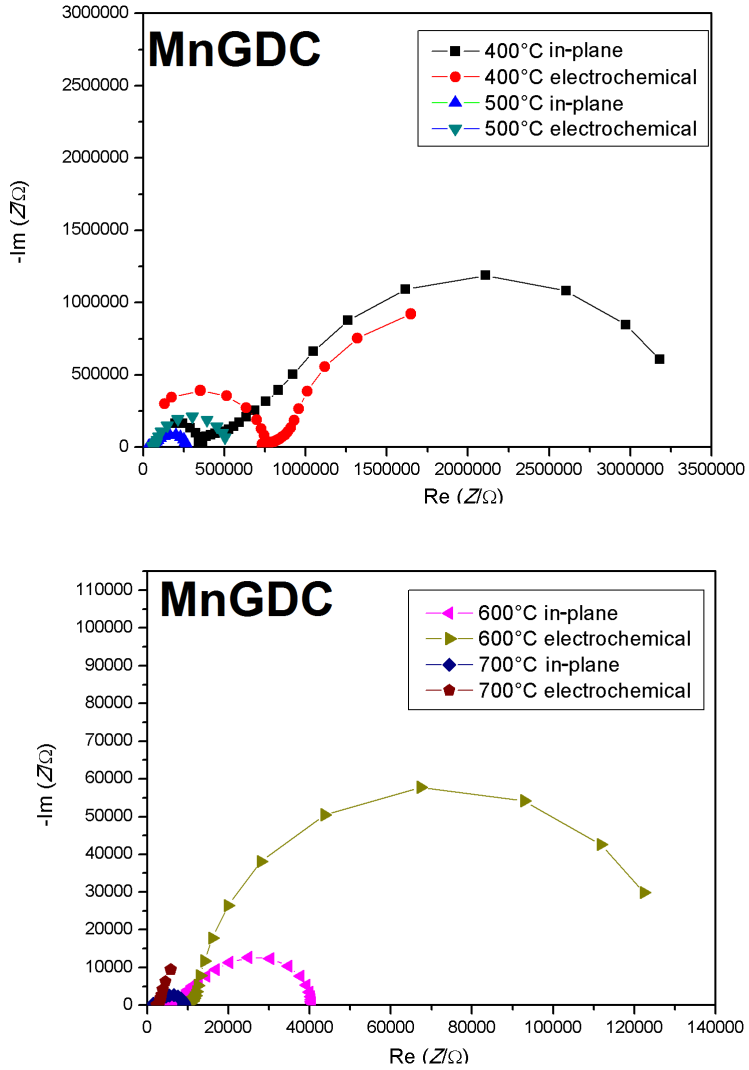

Figure 5.5: Temperature dependence of the spectra - EIS spectra measured at different set temperatures (MnGDC, 11.7 μm finger distance, buried current collectors).

shown, including the results from a linear regression of the data points in both directions (temperature up and down).

One can see that the slopes of the lines are different for the heating and cooling cycle. Acitvation energies are 1.37 eV and 1.16 eV for $R_{\text{electronic}}$ and 1.06 eV and 0.98 eV for R_{ionic}, respectively. This suggests, that the material had changed while heating and this had a

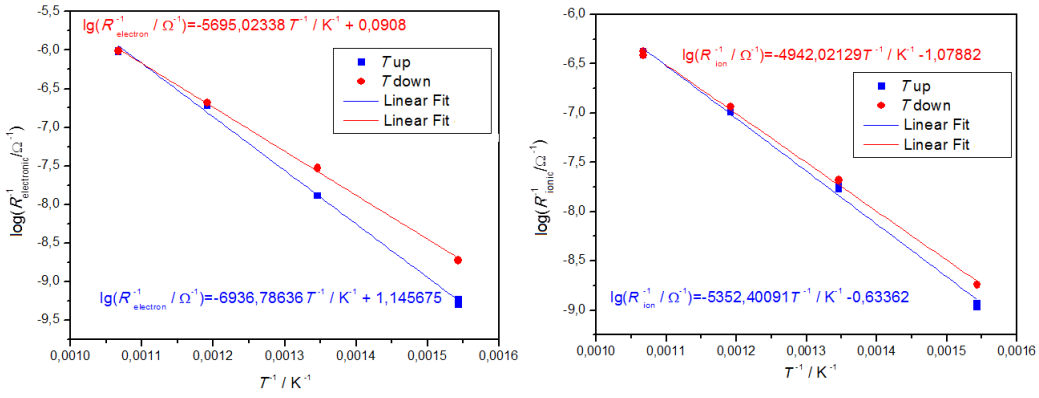

Figure 5.6: Arrhenius plot for $R_{\text{electronic}}$ (electronic sheet resistance) and R_{ionic} ionic sheet resistance, MnGDC micro sample, metal grid beneath the electrode, finger distance: 11.7 μm.

positive influence on the electronic and ionic conductivity. The change is particularly visible in R_{surface}. One representative example for the results of these measurements is shown in Figure 5.7.

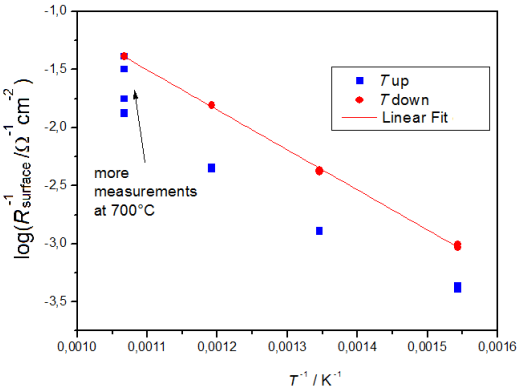

Figure 5.7: Surface resistance values between 400 °C and 700 °C set temperatures and Arrhenius plot for MnGDC micro sample, metal grid beneath the electrode, finger distance: 11.7 μm.

Impedance spectra continuously measured at 700 °C show a decrease of the area specific resistance (a better kinetics), quasi converging to a minimum value within the measured

time interval. This continuous property change did not apply to $R_{\text{electronic}}$ and R_{ionic}. Measurements while cooling down to 400 °C step by step show no change in the activation energy of R_{surface}, as the slope of the line in the cooling direction does not differ from the slope of the line in the heating direction, they run parallel to each other. This suggests, that there is no new reaction paths opened after being kept at 700 °C. The rate limiting process is probably the same, but occurs with a smaller resistivity, for which a structural change in the material can be a possible explanation.

In order to observe the time-dependent variations in surface activity, a further long measurement was carried out at 700 °C, by detecting spectra in five minutes intervals (Figure 5.8, Figure 5.9). An initial decrease with subsequently increasing area specific resistance was observed for MnGDC micro samples (Figure 5.8, Figure 5.9). According to these observations, the following in-depth investigation of MnGDC samples was performed after keeping the sample a few hours at 700 °C to reach the „degradation valley“.

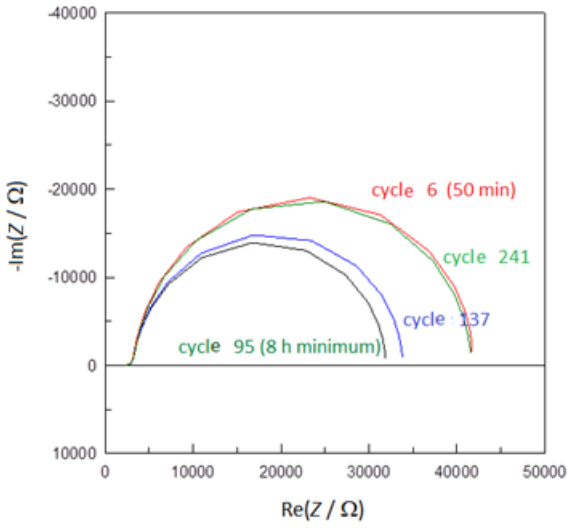

Figure 5.8: Change in the impedance spectra measured on MnGDC micro sample with buried fingers, $d = 11.7$ μm, 26 h measurement at 700 °C set temperature

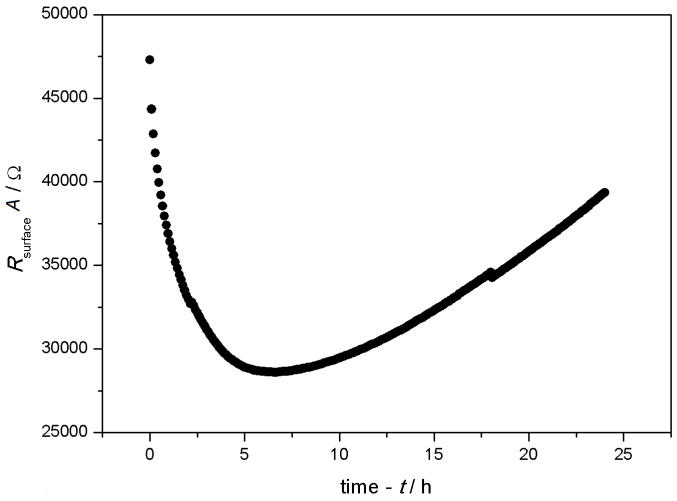

Figure 5.9: Change in surface activity, MnGDC micro sample with buried fingers, 26 h measurement at 700 °C set temperature (A: surface)

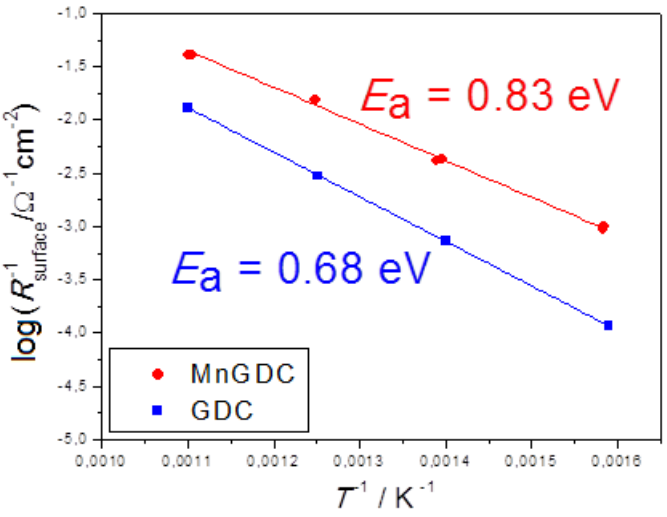

Figure 5.10: Area specific surface resistance for GDC, MnGDC (samples with buried metal grid, 11.7 μm finger distance) - Arrhenius plots between 400 °C and 700 °C set temperatures.

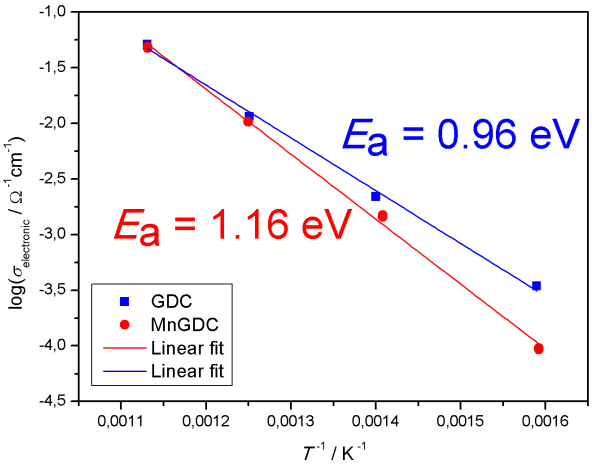

Figure 5.11: Electronic conductivity $\sigma_{\text{electronic}}$ for GDC, MnGDC (samples with buried metal grid, 11.7 μm finger distance) - Arrhenius plots between 400 °C and 700 °C set temperatures.

In Figure 5.10 the area specific surface resistance can be seen for the two materials in Arrhenius plots with the higher MnGDC values of the cool-down process (i.e. in the „degradation valley“). The surface catalytic activity of MnGDC is about half an order of magnitude better than for the material without Mn doping.

The electronic conductivity is presented in Figure 5.11. Although the area specific surface resistance is better for MnGDC, little difference was found in the electronic conductivity at 700 °C, the co-doped material is even worse regarding the electronic conductivity at lower temperatures. This can be explained by the so called polaron hopping mechanism, which will be discussed in greater details in Section 5.5.

The evaluation of the Arrhenius plot for chemical capacitances showed that this property depends on temperature, however it is not simply Arrhenius activated, particularly in the low temperature range. Hence the corresponding activation energies should be taken woth care (Figure 5.12). In ceria, the chemical capacitance characterises the amount of Ce^{3+} ions (see Section 5.5) and is a bulk property. Hencewe can assume that the largest

difference of the two materials (largest difference of the measured parameters) should be found on the surface. This is also in good agreement with the findings of the SEM-analysis.

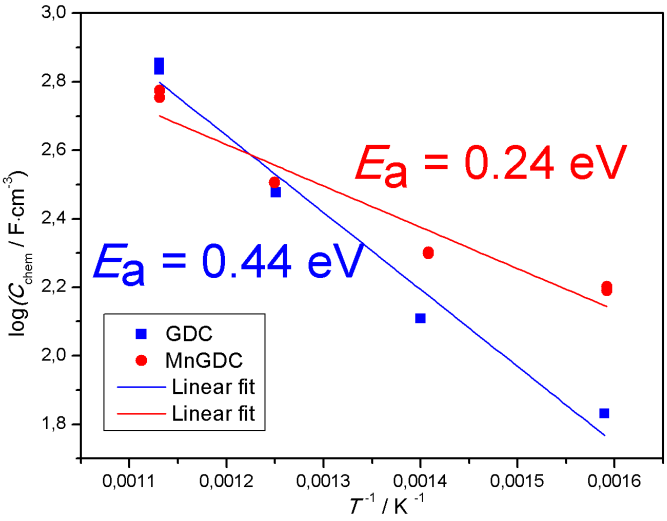

Figure 5.12: Chemical capacitance depending on temperature, GDC and MnGDC micro samples, buried metal fingers, 11.7 μm finger distance.

For comparison, the mean calculated activation energies for electronic and ionic conductivity and the activity of the surface reaction are summarised in Table 5.1, where values are averaged over several samples.

Material property	$\bar{E}_a$/eV GDC	$\bar{E}_a$/eV MnGDC
Electronic conductivity	0.96	1.16
Ionic conductivity	1.06	0.98
Surface reaction	0.68	0.83

Table 5.1: Mean values of the activation energies of the different electrode properties with current collector beneath the electrode

In Table 5.2 the material features calculated by extrapolation of all measurements to

$T = 700$ °C are summarised. Please note, that the mean of relative errors, defined by

$$MRE = \sqrt{\sum_{\text{fitpoints}} \frac{\left(Z_{\text{measured}} - Z_{\text{fit}}\right)^2}{Z^2_{\text{measured}}}} \tag{5.2}$$

was minimised. The confidence intervals were calculated by use of the Student's t-distribution. From these values it can clearly be seen, that in respect of the surface catalytic activity

Property	GDC	MnGDC
$R_{\text{surface}}/\Omega\text{cm}^2$	(49.1 ± 5.7)	(21.5 ± 1.9)
$\sigma_{\text{electronic}}/\text{Scm}^{-1}$	(0.150 ± 0.033)	(0.165 ± 0.038)
$\sigma_{\text{ionic}}/\text{Scm}^{-1}$	(0.0505 ± 0.0097)	(0.0348 ± 0.0067)

Table 5.2: Material properties deduced from the fit procedure for $T = 700$ °C

MnGDC seems to be better. In the electronic conductivity (at least at $T = 700$ °C set temperature) there is no significant difference, while for the ion conduction GDC exhibits the higher value. The slightly worse ionic conductivity of the Mn co-doped material in spite of the higher dopant amount was also experienced by [8], where it was explained by Mn diffusion in the material during operation at high temperature, causing deterioration of the total conductivity.

Macro samples

Figure 5.13 illustrates the temperature dependence of the measured impedance spectra for macro samples. As mentioned in Section 4.3, all of these spectra were fitted by the simplified equivalent circiut model, shown in Figure 4.5 and the area-specific value of R_2 is interpreted as R_{surface}. The appropriateness of this model for fitting is presented in Figure 5.14.

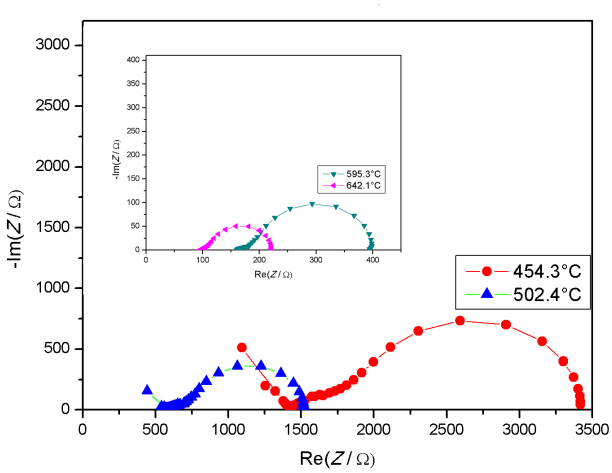

Figure 5.13: Temperature dependence of the spectra - EIS spectra measured at different temperatures (MnGDC macro sample, buried current collectors).

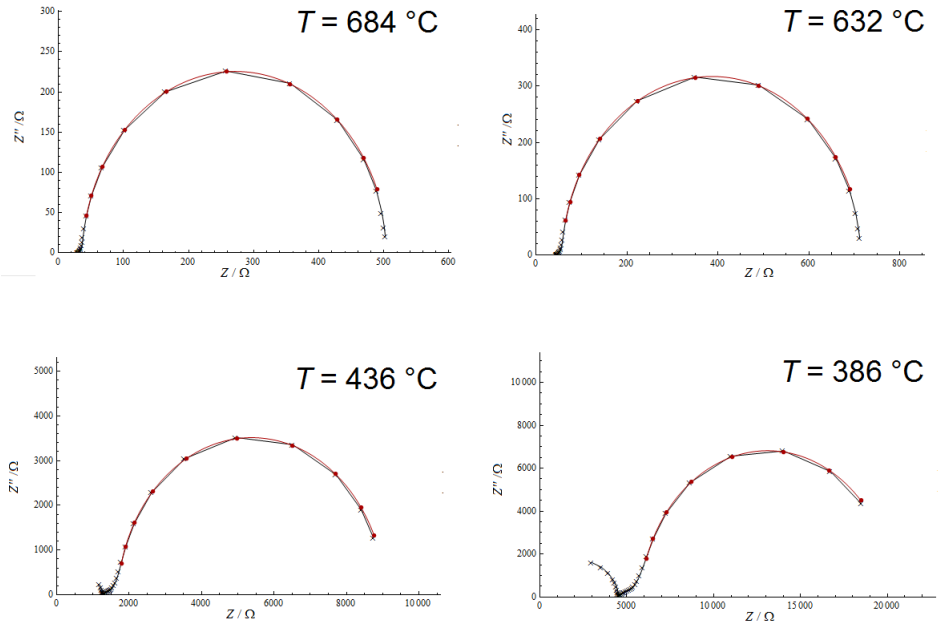

Figure 5.14: Examples for fitting of macro spectra at different temperatures (MnGDC macro sample with buried metal grids) by means of the simplified equivalent circuit of Figure 4.5.

In Figure 5.15 and Figure 5.16 the resulting resistances of the macro measurements are shown for GDC and MnGDC.

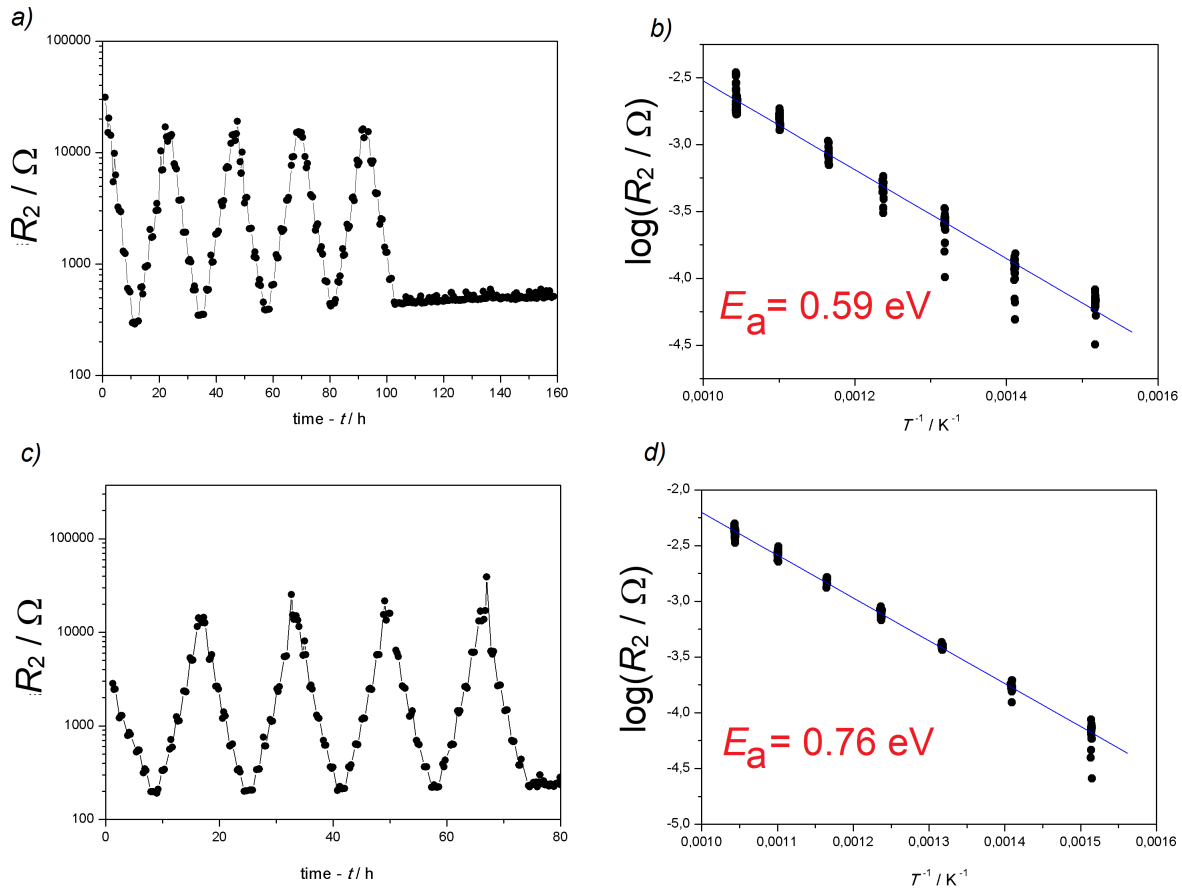

Figure 5.15: Results of macro measurements on GDC: a) Variation of the surface exchange activity (corresponding to R_2 in Figure 4.5) in temperature cycles between 400 °C and 700 °C, buried metal grid; b) Arrhenius plot, buried metal grid; c) Variation of the surface exchange activity in same temperature cycles for metal grid on top; d) Arrhenius plot for metal grid on top.

On the basis of Figure 5.16 and Figure 5.15 it can clearly be seen, that in respect of the area specific resistance ($R_{\text{surface}} \approx R_2 \cdot A$, where A is the effective surface of the macro sample) MnGDC is lower by a factor of ca. 2.5. This also shows a better catalytic activity for MnGDC. Furthermore, one can see that the platinum grid has an additional catalytic

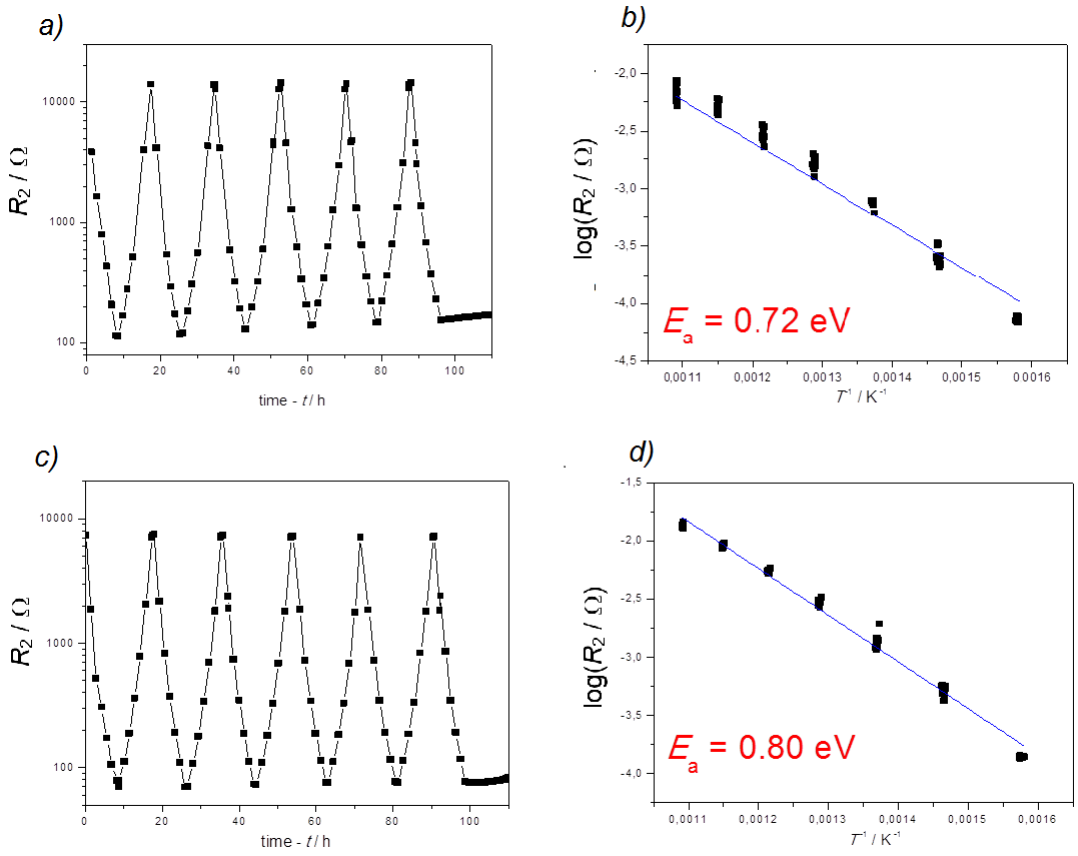

Figure 5.16: Results of macro measurements on MnGDC: a) Variation of the surface exchange activity (corresponding to R_2 in Figure 4.5) in temperature cycles between 400 °C and 700 °C, buried metal grid; b) Arrhenius plot, buried metal grid; c) Variation of the surface exchange activity in same temperature cycles for metal grid on top; d) Arrhenius plot for metal grid on top.

effect, as the area specific resistance is always better for samples with top current collectors despite of the fact, that in this case less MIEC-area is exposed to the gas. Samples with Pt grid on top also showed a slightly higher activtion energy. These findings are besides in good agreement with the result of the macro samples, see Table 5.3. Moreover, the macro samples showed less degradation, which makes a long and reproducible measurement possible. Therefore these samples are particularly suitable for comparison of

materials, evaluation of kinetic and thermodynamic effects, investigation of the effects of the crystallographic orientation (see below) etc.

Property	GDC	MnGDC
Micro $R_{\text{surface}}/\Omega\text{cm}^2$	(49.1 ± 5.7)	(21.5 ± 1.9)
Macro $R_{\text{surface}} \approx R_2 A/\Omega\text{cm}^2$	103.2	23.7

Table 5.3: Comparison of the surface exchange activity determined from micro and macro measurements for $T = 700$ °C

5.3 Scanning electron microscopy, SEM

GDC and MnGDC samples which were measured by impedance spectroscopy and thus exposed to a high temperature and even temperature cycling were characterised by scanning electron microscopy.

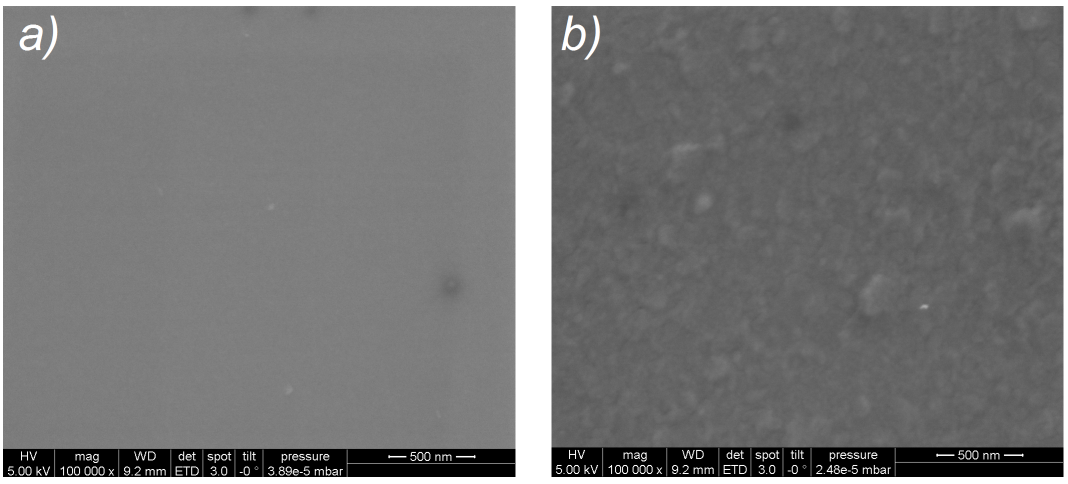

Figure 5.17: SEM top-views of 200 nm GDC deposited on YSZ, a) after PLD, b) after heating up to 700 °C for about 20 hours.

As it can be seen in Figure 5.17 and Figure 5.18, the freshly deposited thin films are flat, without any visible grains. After measuring the samples, MnGDC tends to form

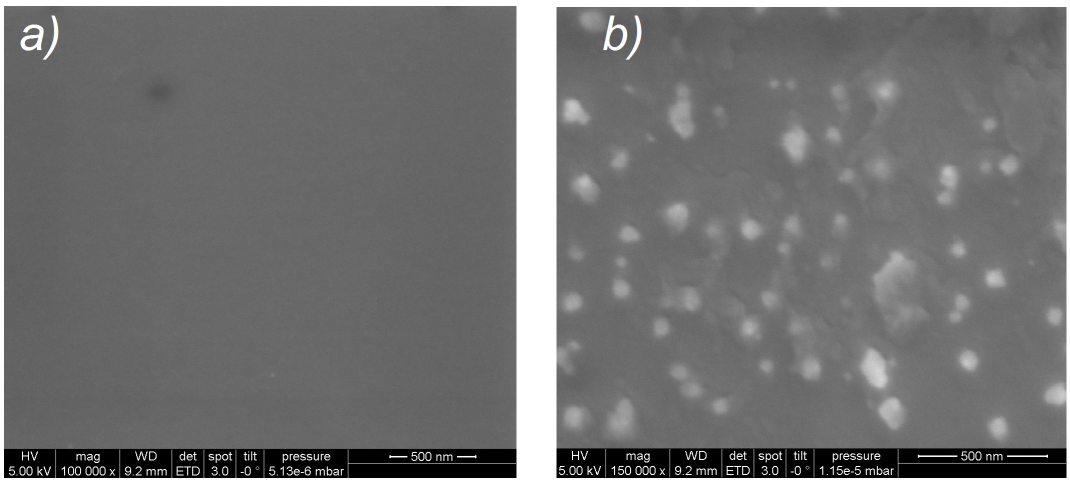

Figure 5.18: SEM top-views of 200 nm MnGDC deposited on YSZ, a) after PLD, b) after heating up to 700 °C for 26 hours

precipitations (segregations) on the surface, which most probably have an influence on the surface catalytic activity. This can explain the observation, that the chemical capacitance as a bulk property does not differ much for GDC and MnGDC while the surface exchange becomes much better for MnGDC.

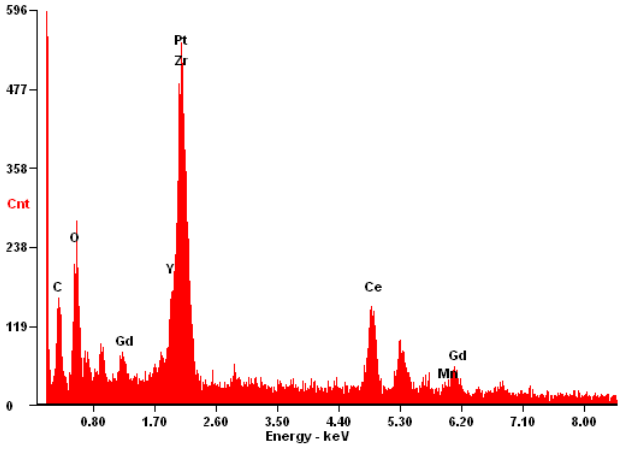

Figure 5.19: EDX analysis of a 200 nm MnGDC thin film on YSZ single crystal

In EDX measurements (Energy dispersive X-ray spectroscopy) on the same thin films of MnGDC, we had difficulty to unambiguously see the prescence of manganese (Figure 5.19).

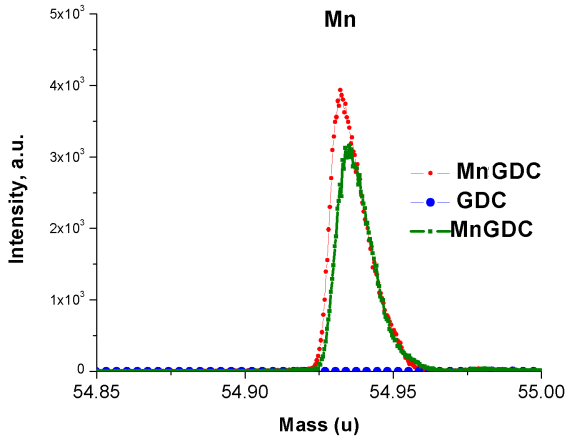

Figure 5.20: Depth profiling analysis of MnGDC thin film on YSZ single crystal. As it can be clearly seen, in the MnGDC samples there is a huge peak at the atomic mass of Mn, in contrast to GDC, which proves the prescence of Mn in the film. The two curves are for different measuring positions.

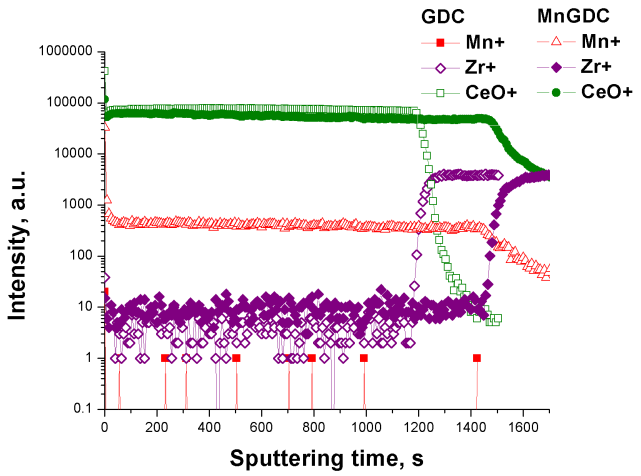

Figure 5.21: Depth profiling analysis of GDC and MnGDC thin layers on YSZ single crystal. The GDC sample contains no Mn, the MnGDC sample contains it in a constant concentration through the layer

With SIMS (Secondary Ion Mass Spectrometry) depth profiling analysis, however, it can be clearly stated, that these thin films contained Mn (Figure 5.20) in a constant concentration through the film (Figure 5.21). One has to mention, that the different sputter times until the onset of the Zr^+ of the two different samples may be due to the different sputtering mechanism or matrix effects.

5.4 Current-voltage characteristics

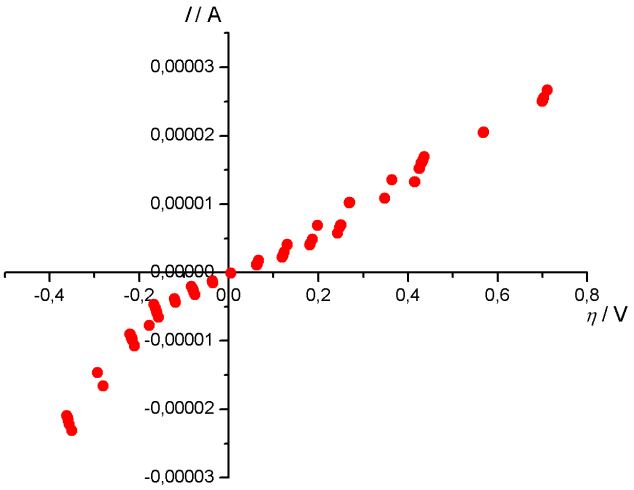

Figure 5.22: Current-voltage diagram for a micro MnGDC sample, T=700 °C set temperature. η is the overpotential, calculated by $\eta = U - IR_{\mathrm{YSZ}}$, where U is the applied voltage.

As it was already mentioned, an impedance spectra contains a lot of worthy information about our electrochemical system. We have the additional opportunity to provide EIS measurements with simultaneous polarisation (applied bias voltage, overpotential at the electrode). This way, not only can the current-voltage diagrams be evaluated, but it is also possible to get valuable additional informations about the material for mechanistic

conclusions. For instance, it can be studied whether a material is p- or n-conducting for a given oxygen partial pressure.

On the basis of current-voltage curves it can be further studied, whether the surface reaction follows the Butler-Volmer equation, which can be widely used for the characterisation of kinetics in liquid electrochemistry. This equation is based on two assumptions: firstly, that a charge transfer is the rate limiting step, which can be true for our system. But the second condition, that the overpotential step is at the same location as the charge transfer, is not fulfilled, as we have an insulating atmosphere [23]. As it can be seen in Figure 5.22, the current-voltage curve shows strong non-linearity, but it deviates from the Butler-Volmer kinetics; especially the anodic curve appears more ohmic than exponential.

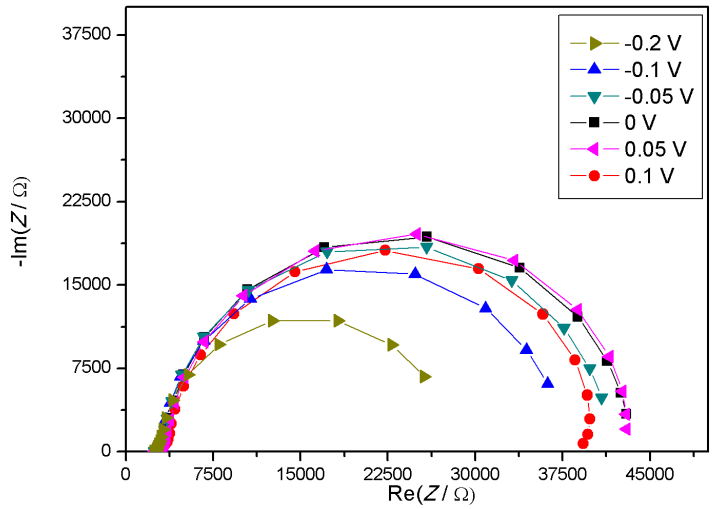

Figure 5.23: Measured impedance spectra upon bias voltage, T=700 °C set temperature, MnGDC micro sample

In Figure 5.23 impedance spectra measured at different bias voltages are demonstrated. As it can be seen, the shape of the spectra depends strongly on the applied bias. The measured impedance spectra were fitted to the simplified equivalent circuit in Figure 4.5.

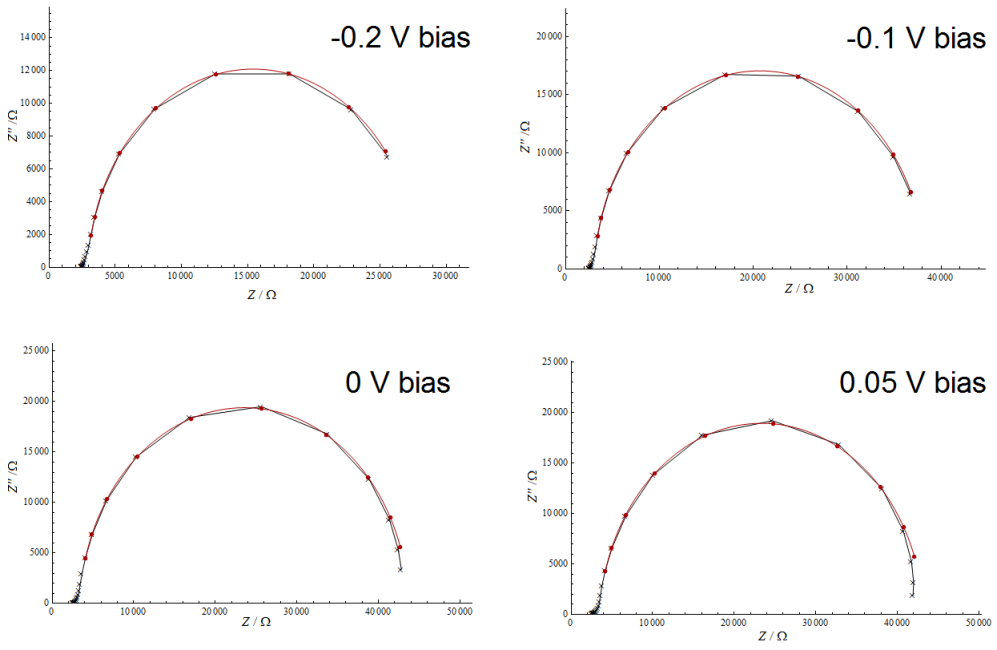

Figure 5.24: Measured spectra of Figure 5.23(black curve) and their fit (red curve).

R_2 mainly expresses the oxygen exchange activity, it is attributed to the surface resistance. Representative examples for the fitting at different bias voltages are presented in Figure 5.24.

The resistive offset R_1 can be used as an indication for resistive processes occuring apart from the surface reaction, generally it corresponds to the ionic and electronic losses in material. For instance, if R_1 is close to the high frequency interceot (R_{YSZ}) while $P \longrightarrow 1$ (so $T \longrightarrow C$, the capacitance is more or less ideal), it can be assumed, that the surface reaction is dominating, while $R_1 \gg R_{\mathrm{YSZ}}$ and a strongly non-ideal capacitance suggests that other processes may be equally relevant.

As it was mentioned in Section 4.3, the chemical capacitance is a property that is in a close relationship with the accumulated charged defects in the material. This property may thus give information about the defect concentration in the material; moreover in the case of doped ceria it is proportional to the Ce^{3+} concentration, see Section 5.5.

As visible from Figure 5.25, the chemical capacitance strongly depends on the applied

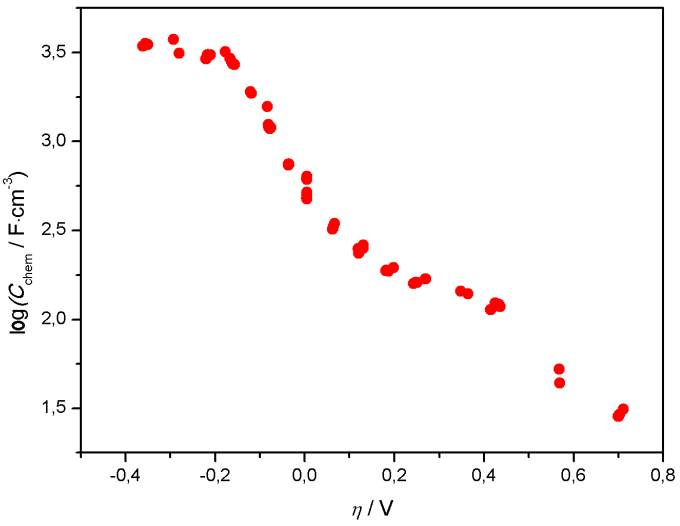

Figure 5.25: $\log C_{\text{chem}}$ vs. applied overpotential ($\eta = U - IR_{\text{YSZ}}$) , $T = 700°\text{C}$ set temperature, MnGDC micro sample

DC-bias. It increases with negative overpotential, converging to a maximum, while in the anodic region (positive overpotential) a continuous decrease of C_{chem} can be observed. For the interpretation we can use the Nernst-equation:

$$\eta = \frac{RT}{zF} \ln \frac{p_{\text{O}_2,\text{atmosphere}}}{p_{\text{O}_2,\text{bulk}}} \tag{5.3}$$

which makes a relationship between the applied overpotential and the oxygen partial pressure in the electrode. In that way, a p_{O_2} scale can be derived from the η scale. The η scale is a logarithmic scale for the oxygen partial pressure. According to [24] the chemical capacitance of ceria is proportional to the Ce^{3+} concentration, which represents the electron concentration. So, the logarithmic C_{chem} vs. η plot shows, that ceria is actually in the n-conducting regime of the Brouwer diagram: the electronic charge carrier concentration increases with decreasing p_{O_2}. According to these thoughts, the steep slope in the plot confirms, that doped ceria is a better electronic conductor if the athmosphere is more reducing. This plot is also a proof, that in this measurement the MIEC layer is really

polarised and the defect chemistry of the material changes in dependence of the potential.

It has to be mentioned, that the plateau at higher negative bias does not necessarily reflect a material feature, as at these bias values it is not sure, whether the electrode is homogenously polarised. It is even more plausible, that the fitting model does not work reliably.

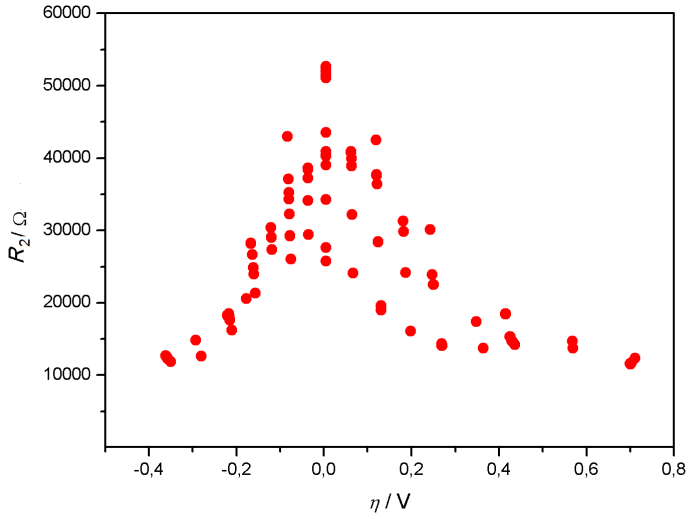

Figure 5.26: Surface activity vs. applied overpotential, $T = 700°C$

The surface activity related resistance R_2 corresponding to Figure **??** is plotted in Figure 5.26. It can be clearly seen, that it has a maximum value at $\eta = 0$ which indicates that the kinetics becomes better with positive as well as with negative overpotential.

5.5 Electronic conduction in GDC, polaron hopping

Electronic conduction in gadolinium doped and gadolinium/manganase co-doped ceria takes place by the so called polaron hopping process as in the case of pure ceria [25]: under low oxygen pressures (so in reducing atmosphere as for the measurements in this

work) not only oxygen vacancies (ionic conductivity) but also electronic defects (small polarons) are relevant for the transport properties of the material, as the present Ce^{4+} ion can be easily reduced to Ce^{3+} according to ([26]):

$$Ce^{4+} + e^{-} \longrightarrow Ce^{3+} \tag{5.4}$$

Using the Kröger-Vink notation this can be written as

$$2Ce_{Ce}^{\times} + O_{O}^{\times} \longrightarrow \frac{1}{2}O_2 + 2Ce_{Ce}^{\prime} + V_{O}^{\bullet\bullet} \tag{5.5}$$

Actually, this reduced cation can be treated as an electron sitting in an energy minimum, confined to an atom (to its self-induced ionic displacement field and lattice distortion opposed to an electron in the conduction band) [27]. This is a small polaron that can be transported via a thermally activated process [28] and the process is called polaron hopping, resulting in electronic conduction in the material (including the motion of the lattice distortion). According to [11], the formation of such a small polaron is physically equivalent to an infinitesimal change in non-stoichiometry:

$$\lim_{\alpha \to 0} \frac{1}{2}O_2(g) + \frac{1}{\alpha}M_xCe_{1-x}O_{2-\frac{x}{2}-\delta-\alpha} \rightleftharpoons \frac{1}{\alpha}M_xCe_{1-x}O_{2-\frac{x}{2}-\delta} \tag{5.6}$$

where M is a trivalent dopant (manganese, gadolinium) with doping level x. This means, that the concentration of electrons being transported is equal to the concentration of Ce^{3+}:

$$\left[Ce^{3+}\right] = c_{\text{electron}} \tag{5.7}$$

It is possible to determine (calculate) the activation energy of the polaron hopping process in GDC by using the measured electronic resistance and the chemical capacitance. According to [29], the volume specific chemical capacitance (for a homogenous thin film with volume V) allocated to the carrier i can be written as

$$C_{\text{chem},i} = (ez_i)^2 \left(\frac{\partial \mu_i}{\partial n_i}\right)^{-1} \tag{5.8}$$

Equation (5.8) can be reconsidered for a MIEC with electrons and oxygen vacancies. In the case of GDC, one can write:

$$C_{\text{chem}} = 4e^2 \left(\frac{\partial \mu_{\text{O}}}{\partial n_{\text{O}}} \right)^{-1} \tag{5.9}$$

The chemical potential of oxygen can be expressed by

$$\mu_{\text{O}} = \mu_{\text{O}^{2-}} - 2\mu_{\text{e}^-} = -\mu_{\text{V}_{\text{O}}^{\bullet\bullet}} - 2\mu_{\text{e}^-} \tag{5.10}$$

By taking the charge neutrality and the lattice site conservation into consideration:

$$dn_{\text{O}} = -dn_{\text{V}_{\text{O}}^{\bullet\bullet}} = -\frac{1}{2} dn_{\text{e}^-} \tag{5.11}$$

$$\Longrightarrow C_{\text{chem}} = 4e^2 \left(\frac{\partial \mu_{\text{V}_{\text{O}}^{\bullet\bullet}}}{\partial n_{\text{V}_{\text{O}}^{\bullet\bullet}}} + 4 \frac{\partial \mu_{\text{e}^-}}{\partial n_{\text{e}^-}} \right)^{-1} \tag{5.12}$$

With $\mu_i = \mu_i^{\ominus} + kT \ln \frac{n_i}{n_i^{\ominus}}$ where $n_i^{\ominus}$ is the standard concentration:

$$\Longrightarrow C_{\text{chem}} = \frac{4e^2}{kT} \left(\frac{1}{n_{\text{V}_{\text{O}}^{\bullet\bullet}}} + \frac{4}{n_{\text{e}^-}} \right) \tag{5.13}$$

for $n_{\text{V}_{\text{O}}^{\bullet\bullet}} \gg n_{\text{e}^-}$

$$C_{\text{chem}} = \frac{e^2 n_{\text{e}^-}}{kT} \tag{5.14}$$

By substituting Equation (5.7) we get:

$$C_{\text{chem}} = \frac{e^2 \left[\text{Ce}^{3+}\right]}{kT} \tag{5.15}$$

This formula requires some preconditions (Equation (5.16), Equation (5.17)), which have to be filled, otherwise also other charge carriers should be included and the calculation would be more complicated.

$$\frac{\left[\text{Ce}^{3+}\right]}{\left[\text{Ce}^{4+}\right]} \ll 1 \tag{5.16}$$

and

$$\frac{\left[\text{Ce}^{3+}\right]}{\left[\text{V}_{\text{O}}^{\bullet\bullet}\right]} \ll 1 \tag{5.17}$$

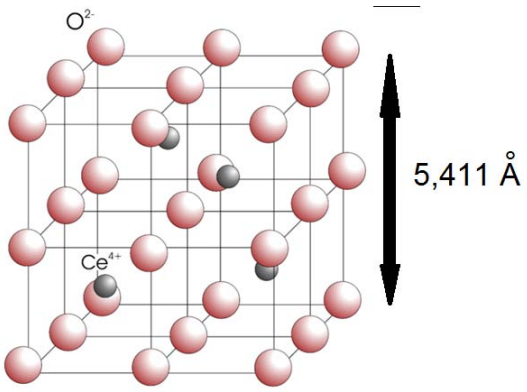

Figure 5.27: Unit cell of ceria

The validity of the prerequisites of Equation (5.15), given by Equation (5.16) and Equation (5.17) shown as follows: CeO_2 has a cubic crystal structure (Figure 5.27) and a lattice parameter of 0.5411 nm, its unit cell contains 4 Ce-ions. The total Ce concentration is

$$[\mathrm{Ce}]_{\mathrm{total}} = \frac{N_{\mathrm{Ce\ per\ unit\ cell}}}{V_{\mathrm{unit\ cell}}} = \frac{N_{\mathrm{Ce\ per\ unit\ cell}}}{d^3} = \frac{4}{(5,411 \cdot 10^{-8}\ \mathrm{cm})^3} = 2,52 \cdot 10^{22} \frac{1}{\mathrm{cm}^3} \quad (5.18)$$

This value can be taken as the number of cation sites also for the doped material. Since only 80% of the cations are Ce ions we get $[\mathrm{Ce}]_{\mathrm{GDC,\ total}} = 2,016 \cdot 10^{22} \frac{1}{\mathrm{cm}^3}$.

In our calculations according to Equation (5.15) $10^{18} \frac{1}{\mathrm{cm}^3} < \left[\mathrm{Ce}^{3+}\right] < 10^{20} \frac{1}{\mathrm{cm}^3}$ is found in the temperature range considered here and thus $n_{\mathrm{electron}} = \left[\mathrm{Ce}^{3+}\right] \ll [\mathrm{Ce}]_{\mathrm{GDC,\ total}}$ is fulfilled.

Because of interfacial capacitances the chemical capacitance calculated by fitting is not exactly the same as the chemical capacitance given by Equation (5.15). However, a correction term is not known, so the fit values were used for the further calculations.

The mobility u_{electron} can be calculated from the measured electronic conductivity $\sigma_{\mathrm{electron}}$ according to:

$$\sigma_{\mathrm{electron}} = e u_{\mathrm{electron}} \left[\mathrm{Ce}^{3+}\right] \quad (5.19)$$

For the investigation of the activation energy, it has to be taken into consideration that the thermal activation of the conductivity is not equivalent to that of the mobility, since the concentration of charge carriers (defects) also changes with the temperature. Moreover, as shown by Holstein and Friedmann ([30], [31]), the temperature-dependence is given by (Figure 5.28):

$$u_{\text{electron}} = \frac{u_{\text{electron},0}}{T} \cdot \exp\left(-\frac{E_{\text{a}}}{kT}\right) \tag{5.20}$$

where E_{a} is the activation energy for the hopping process in relation with the polaron binding energy E_n according to Equation (5.21) (Marcus-theory, [32]), $u_{\text{electron},0}$ is a constant including properties characterizing lattice vibrations (phonons).

$$E_{\text{a}} = \frac{1}{2}E_n \tag{5.21}$$

E_n is the energy difference between the two, +3 and +4 oxidation states. The activation

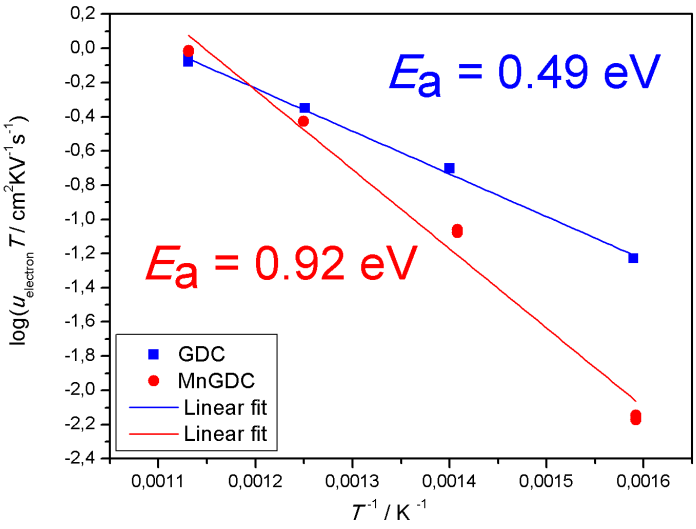

Figure 5.28: Arrhenius plot for polaron hopping process in GDC

energies can be determined from the $\log(u_{\text{electron}}T)$ vs. $\frac{1}{T}$ data plot, Figure 5.28 with

$$u_{\text{electron}} = \frac{\sigma_{\text{electron}}e}{kTC_{\text{chem}}} \tag{5.22}$$

The activation energy calculated for GDC (0.49 eV) is a realistic value, while that for MnGDC (0.92 eV) is too high for an activation energy of a polaron hopping process. This suggests, that in the chemical capacitance also the concentration of Mn-ions should be taken into considerations, as Mn provides another trapping centre for electrons: also the Mn(III)-Mn(II) valence change occurs, and the chemical capacitance is no more a measure for the Ce^{3+} concentration. This, of course, hinders the polaron hopping due to the small concentration of Mn ions in contrast to that of the Ce-ions: Mn cannot form chains for electron jumping, in most of the cases the electron has to jump from a Mn to a Ce-ion. According to this interpretation the activation enthalpy of the process of electron jumps from Mn to Ce should be considerably larger than for Ce-Ce jumps. This was not measured so far, but NIR-VIS absorption spectroscopy may resolve the energy difference between Ce'_{Ce} and Mn'_{Ce}. Furthermore, it has to be stated, that because of the limited solubility of Mn in the ceria lattice most probably also some other processes contribute to the chemical capacitance, e.g. exchange between different phases etc.

5.6 Possible reaction paths on MnGDC

For the investigation of the possible reaction paths on MnGDC the following series of experiments was carried out.

Step 1 At first, a MnGDC sample was preparated with metal grid on the top of the electrode, but in this case without micro-structuring the thin layer. This way the MnGDC-film beneath the metal fingers was flat without any rectangular micro electrodes. The sample was characterised by impedance spectroscopy in the usual way.

Step 2 Secondly, the sample was left in the laboratory and after 2 months was measured again.

Step 3 Subsequently, also the thin layer was micro-structured, but now by use of the negative fingers on the lithographic mask. In this way, almost the whole area of the ceramic

thin film (electrodes) was covered with metal fingers. (In the following, the measurement steps will be indicated with the numbers *1*, *2* and *3*, corresponding to those in the text.) The sample preparation and experiment steps with the possible reaction paths are shown in Figure 5.29.

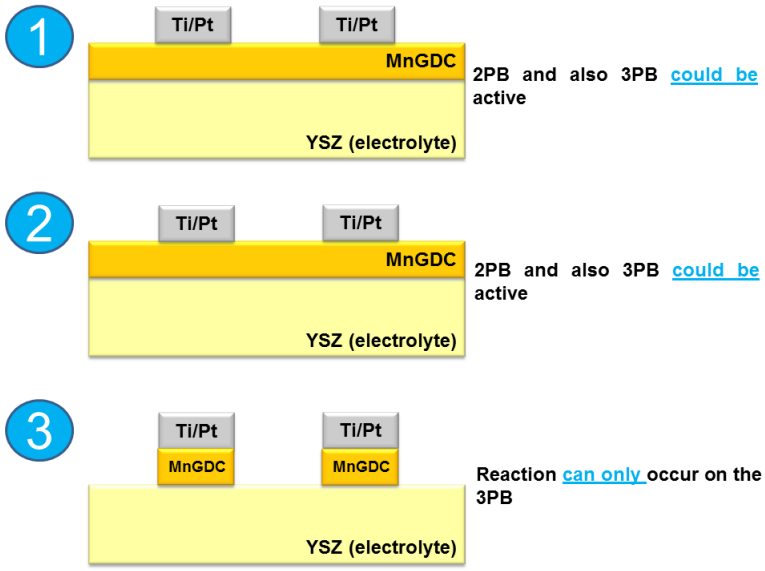

Figure 5.29: Experimental scheme for investigation of possible reaction paths on MnGDC (The numbers correspond to those in the text).

Interpretation of the EIS measurements

In step 1 and step 2, the impedance spectra were fitted by the simplified model mentioned in Section 4.3 in order to obtain the area specific resistance. In step 3, in-plane and the electrochemical measurements were separately fitted to the simplified model (see Figure 4.5) and thus the triple phase boundary activity can be calculated (Equation (5.23)), based on the assumption, that in *step 3* only the triple phase boundary is active, with no other way, by which a reaction could occur.

$$R_{\mathrm{TPB}} = R_{\mathrm{sc}} \cdot k \tag{5.23}$$

where R_{sc} is the diameter of the dominating semicircle (resistance of the electrode) and k is the circumference of fingers.

To investigate the triple phase boundary (surface path) or the two phase boundary (bulk path) activity, it is worth plotting the area specific resistance against the finger distance or the triple phase boundary density, quantified e.g. with the formula $\varrho_{\mathrm{TPB}} = 2 \cdot \frac{1}{d_{\mathrm{finger}}}$. It expresses that there are 2 fingers in each d_{finger} distance. If R_{surface} depends on the geometry, so if the conduction is better with increasing triple phase boundary density, it means that the material is (also) triple phase active. As already mentioned in Section 4.3, triple and two phase activity can not be mechanistically separated, a geometry dependence of R_{surface} does not mean necessarily, that the reaction occurs after adsorption of hydrogen on the surface followed by its surface diffusion to the triple phase boundary.

As it can be seen in Figure 5.30, for *step 1* the area specific resistance depends on the triple phase boundary density, while for *step 2* it is no more depending on the number of the fingers. This result can be interpreted by the assumption, that in *step 1* the two phase boundary and also the triple phase boundary is active, whereas in *step 2* only the two phase activity remained. As possible reason adsorption or segregation processes can be mentioned, which take place on the triple phase boundary, blocking its activity.

In *step 1*, the effective resistance (the measured one) should be an equivalent resistance of parallel resistors, as written in Equation (5.24).

$$\frac{1}{R_{\mathrm{eff}}} = \frac{1}{R_{\mathrm{TPB}}} + \frac{1}{R_{\mathrm{2PB}}} \tag{5.24}$$

The reciprocal of the effective area specific resistance is plotted against the triple phase boundary density in Figure 5.30, for *step 1* and *step 2*, and both of them were interpolated by a linear relation. As it can be seen, $\frac{1}{R_{\mathrm{surface,eff}}}$ is approximately constant as a function of ϱ_{TPB}: $\frac{1}{R_{\mathrm{surface,eff}}/\Omega\mathrm{cm}^2} \approx 0,04477$ for *step 2*. The linear regression of *step 1* provides a

linear relationship between $\frac{1}{R_{\text{surface,eff}}}$ and ϱ_{TPB} according to:

$$\frac{1}{R_{\text{surface,eff}}/\Omega\text{cm}^2} = 1,97731 \cdot 10^{-5}\varrho_{\text{TPB}} + 0,03362 \tag{5.25}$$

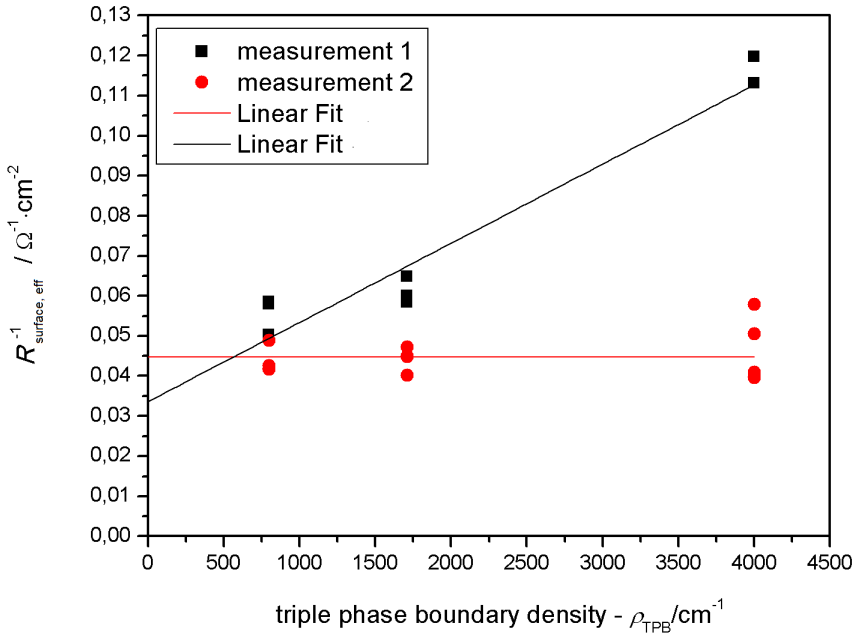

Figure 5.30: Relation between the area specific polarisation resistance of MnGDC, $R_{\text{surface,eff}}$ and the triple phase boundary density, $T = 700$ °C set temperature.

The two lines intercept approximately at $(\varrho_{\text{TPB}} = 563\frac{1}{\text{cm}}; R^{-1}_{\text{surface,eff}} = 0.04477\frac{1}{\Omega\text{cm}^2})$ which renders an effective resistance of $22.3\Omega\text{cm}^2$. This value corresponds to the mean value of the area specific resistances evaluated for *step 2*, for different finger distances $((21.8 \pm 1.4)\Omega\text{cm}^2)$. The difference of *step 1* and *step 2* can therefore be attributed only to the triple phase boundary activity (as $\lim_{\varrho_{\text{TPB}}\to 0} R_{\text{surface,eff}} \approx R_{\text{surface,2PB}}$) and the slope of the fit for *step 1* can be treated as a measure for the triple phase boundary activity. (Theoretically, the two lines should intercept at $\left(0; \frac{1}{R_{\text{surface,eff}}}\right)$ with this assumption,

which is not the case probably because of the statistical uncertainty of measurements.) Taking into consideration that in *step 3* the reaction can only occur on the triple phase boundary, the resistance calculated by means of the linear regression and the one measured in *step 3* should be similar. These values can be seen in Table 5.4, supported by statistics.

	triple phase boundary activity - $\frac{1}{\bar{R}_{\mathrm{sc,measured}} l_{\mathrm{TPB}}} / \frac{1}{\Omega\mathrm{cm}}$
$d = 25\ \mu$m	$(2.0 \pm 1.3) \cdot 10^{-5}$
$d = 11.7\ \mu$m	$(1.9 \pm 1.1) \cdot 10^{-5}$
$d = 5\ \mu$m	$(1.8 \pm 1.5) \cdot 10^{-5}$
Slope of linear fit, *step 1*	$1.97731 \cdot 10^{-5}$

Table 5.4: Mean of resistances of MnGDC measured in *step 3*, and calculated from linear fitting of *step 1*, $T = 700$ °C set temperature. 95% confidence intervals were calculated by means of Student t_α and the standard deviation of values σ_n with the formula $\Delta R = t_\alpha \cdot \frac{\sigma_n}{\sqrt{n}}$. *d*: finger distance

These results indicate that in *step 1* the reaction occurs in the very near region to the triple phase boundary (or on the triple phase boundary) and on the two phase boundary). In *step 2*, only two phase activity can be found. After the ion beam etching step, *step 3* exhibits restored triple phase boundary activity, close to the initial value (Table 5.4).

5.7 Investigation of the kinetics on GDC, MnGDC

The results of impedance measurements are expected to also depend on the atmosphere in which they have been carried out. This statement is straightforward, since the concentrations or types of reactive species in the atmosphere vary. However, according to Brouwer-diagrams, also the bulk defect chemistry and thus the conductivity and electrochemical behaviour of an electrode material changes when the partial pressure of oxygen

in the atmosphere is changed. In this section, it will be shown that it is possible to measure the impedance in different reducing atmospheres without varying the oxygen partial pressure. These measurements provide worthy information on the surface reaction, since the bulk defect chemistry stays constant.

At first, the relationship between the polarisation of the electrode and the oxygen partial pressure will be considered. The standard free enthalpy $\Delta_r G^{\ominus}$ of a chemical reaction is related to the equilibrium constant expressed with activities of the species according to Equation (5.26):

$$\Delta_r G^{\ominus} = -RT \ln K_p \tag{5.26}$$

where Kp is the equilibrium constant expressed with the normalised gas pressures, and $\Delta_r G^{\ominus} = \mu^{\ominus}_{H_2O} - \mu^{\ominus}_{H_2} - \frac{1}{2}\mu^{\ominus}_{O_2}$. $\mu_i^{\ominus}$ is the standard chemical potential of species i. Furthermore:

$$K_p = \frac{p_{H_2O}}{p_{H_2} \cdot \sqrt{p_{O_2}}} \tag{5.27}$$

From Equation (5.26):

$$\Delta_r G^{\ominus} = -RT \ln \frac{p_{H_2O}}{p_{H_2} \cdot \sqrt{p_{O_2}}} \tag{5.28}$$

and we get:

$$p_{O_2,gas} = \left(\frac{p_{H_2O}}{p_{H_2}}\right)^2 \cdot \exp\left(-\frac{2\Delta_r G^{\ominus}}{RT}\right) \tag{5.29}$$

In equilibium, the chemical potential of oxygen in the MIEC corresponds to the partial pressure in the gas phase, $p_{O_2,gas}$. Upon voltage, however:

$$\mu_{O_2,WE} - \mu_{O_2,CE} = 2\left(\tilde{\mu}_{O^{2-}},WE - \tilde{\mu}_{O^{2-}},CE\right) - 4\left(\tilde{\mu}_{e^-,WE} - \tilde{\mu}_{e^-,CE}\right) \tag{5.30}$$

(CE: counter electrode, WE: working electrode). In this equation the following relationship for the electrochemical potential of oxygen was applied:

$$\mu_{O_2} = 2\tilde{\mu}_{O^{2-}} - 4\tilde{\mu}_{e^-} \tag{5.31}$$

The electrochemical potential of O^{2-} is homogenous if ohmic losses in the electrolyte are neglected. $\tilde{\mu}_{e^-}$ however differs by the applied voltage:

$$\tilde{\mu}_{e^-,\mathrm{WE}} - \tilde{\mu}_{e^-,\mathrm{CE}} = -F\eta \tag{5.32}$$

Therefore:

$$\mu_{O_2,\mathrm{WE}} - \mu_{O_2,\mathrm{CE}} = 4F\eta \tag{5.33}$$

When counter electrode kinetics is fast:

$$\mu_{O_2,\mathrm{CE}} = \mu_{O_2,\mathrm{gas}} \Longrightarrow p_{O_2,\mathrm{WE}} = p_{O_2,\mathrm{gas}} \exp \frac{4F\eta}{RT} \tag{5.34}$$

These thoughts lead to the following equation:

$$p_{O_2} = \left(\frac{p_{H_2O}}{p_{H_2}}\right)^2 \cdot \exp\left(-\frac{2\Delta_r G^{\ominus} + 4F\eta}{RT}\right) \tag{5.35}$$

This shows, that the oxygen partial pressure p_{O_2} in the electrode changes exponentially with the overpotential while it is also very important that p_{O_2} is determined by the current $\frac{p_{H_2O}}{p_{H_2}}$ ratio. It has to be mentioned, that p_{O_2} is a mathematical feature, which can be defined also for reducing atmosphere, even though there are no O_2 molecules among the reaction partners.

In the present work, impedance spectra of MnGDC and GDC were measured at 700 °C set temperature in different atmospheres by varying the total amount of hydrogen and water in nitrogen and argon carrier gas, while keeping the mixing ratio constant. The measurements were performed by use of a macro device, in which electrochemical measurements can be carried out in different gas mixtures. These mixtures were provided by mass-flow controllers which mix the components.

Humidified 2.5 % H_2 containing Ar and dry N_2 were mixed. If the H_2 containing gas is wet and this mixture is diluted with N_2, the ratio between hydrogen and water remains constant for a given temperature, only their total partial pressure is varied due to mixing. According to Equation (5.35) the oxygen partial pressure, in other words, the chemical

potential of oxygen is constant. In this way no change in bulk thermodynamics can be expected, the defect chemistry is the same for all mixing ratios, consequently the same electrochemical behaviour of the bulk is expected.

In Figure 5.31 the total partial pressure of the reaction partners ($\Sigma p = p_{H_2} + p_{H_2O}$) used in the measurement series can be seen, corresponding to the mixing ratios of the different gases (wet H_2/Ar and N_2).

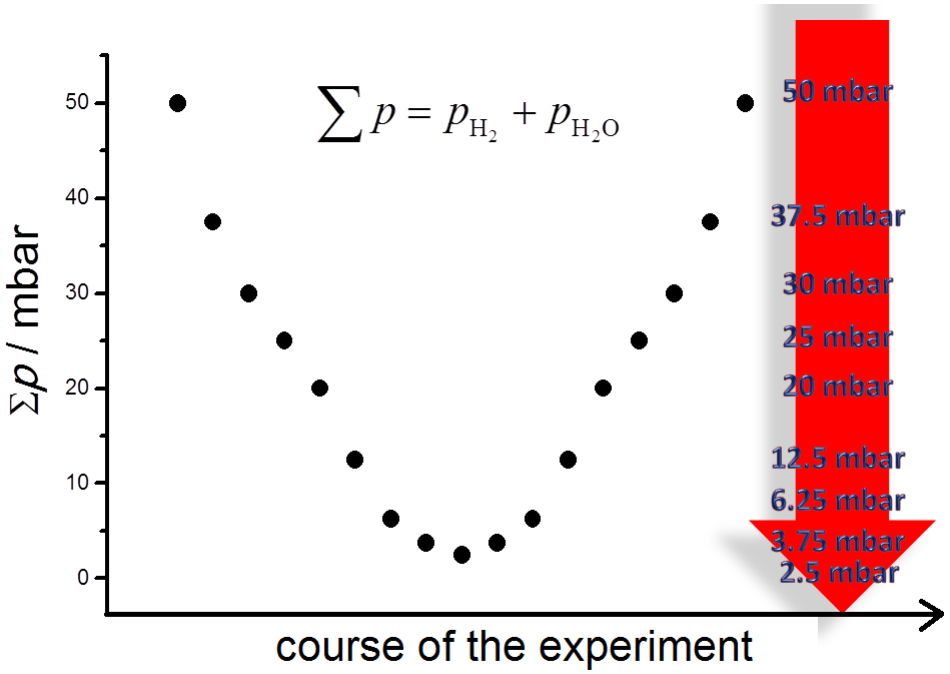

Figure 5.31: Variation of the total partial pressure of reacting gases.

Figure 5.32 shows examples for spectra measured at several total partial pressure values. The spectra were fitted by use of the simplified model mentioned in Section 4.3, Figure 4.5, from which R_2 (interpreted as R_{surface}), $C_{\text{chem}} = \frac{C_2}{Ad}$, where d is the film thickness and (T_{chem} with corresponding p value) could be determined.

Figure 5.33 represents examples for fitting. Figure 5.34 shows the dependence of R_{surface}, according to the simplified fitting model, on Σp in a double logarithmic plot for GDC and MnGDC samples with metal grid on the top and beneath the electrode, respectively.

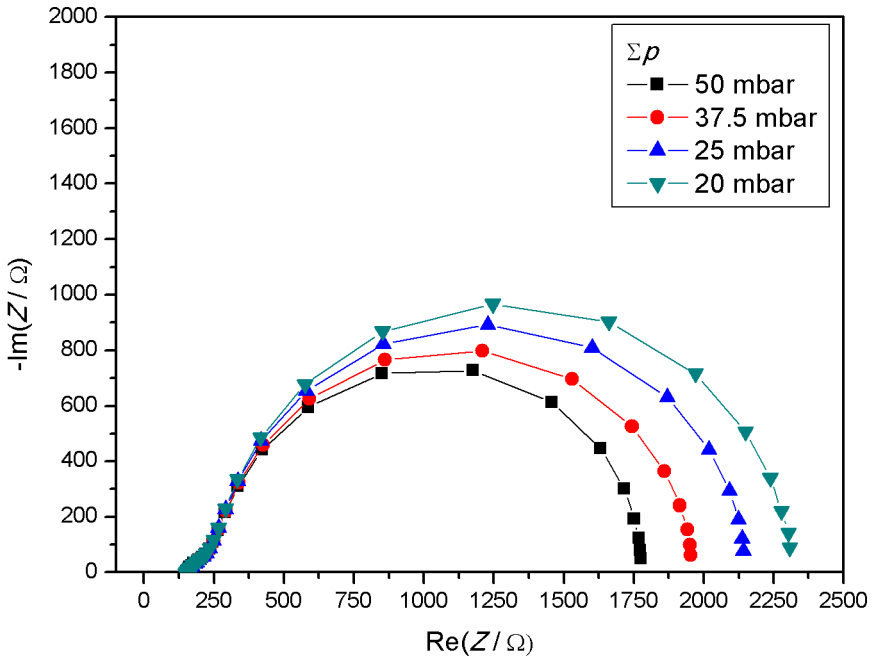

Figure 5.32: Changes in spectra when varying the total partial pressure of reaction partners, measured at 700 °C set temperature on a MnGDC macro sample.

Although the samples with top and bottom metal layers are different, because the top metal layer also has catalytic activity, if one takes either material, their answer to the variation of Σp (in respect of the change in R_{surface}) are pretty well reproducible (slopes are quite the same for a given material). As it can be seen in these plots, variation of the atmosphere without varying of p_{O_2} also has an influence on the resistance of the oxygen exchange: a lower amount of the reaction partners (hydrogen and water molecules) leads to decreased catalytic activity. This behaviour is more pronounced in the case of MnGDC (slope of the lines are higher). These findings may be explained by the assumption, that a process with one of the species (H_2 or H_2O) being involved is the rate limiting step, which is most probably the adsorption of a gas particle on the surface and the following charge transfer. However, p_{H_2O} or p_{H_2} may also influence a preceding reaction in equilibrium and therefore

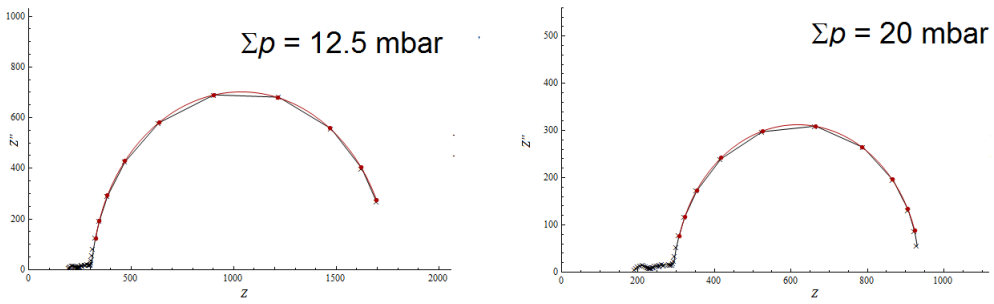

Figure 5.33: Interpretation of the appropriateness of the simplified model for fitting at different total partial pressures. Black curves: measured spectra, red curves: fits. MnGDC macro samples, measured at 700 °C set temperature

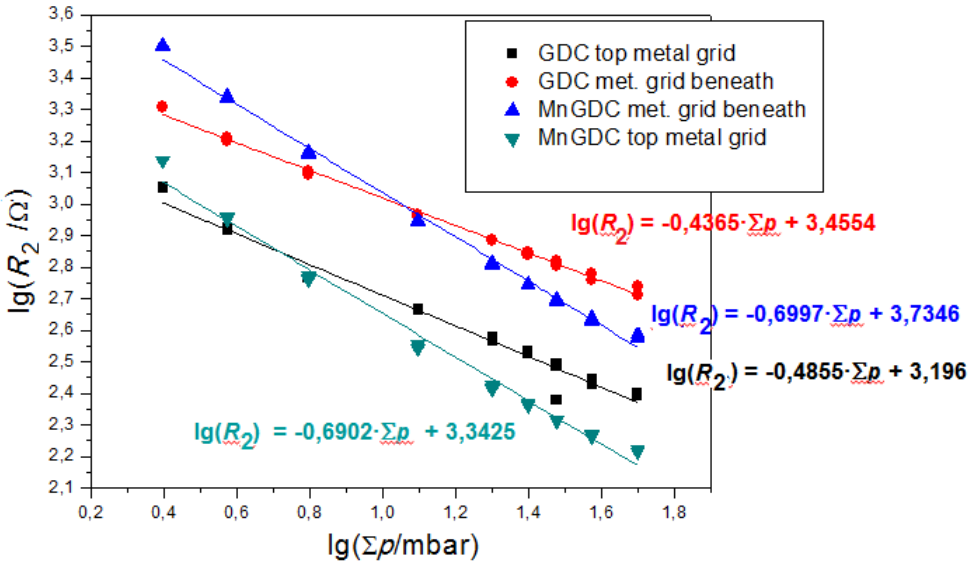

Figure 5.34: Changes in the surface resistance at different total amounts of water and hydrogen.

the concentration of the intermediate is involved in the rate limiting step. Therefore, the change in kinetics can be attributed to the changing total amount of the gas molecules. Of course, from these results it would be extremely complicated to tell which process is rate limiting, how the slopes of the lines in the R_{surface} vs. Σp plots can be interpreted and how they are related to the process. However, by a refinement of such measurements and

the use of surface-sensitive in situ measurement, such as XPS, the rate limiting processes on these materials could be understood, which will be among the further goals of our work. It is, for example also possible to carry out measurements at different oxygen partial pressures, when the concentration of hydrogen and water are varied independently from each other. In this case, we would move along the p_{O_2}-axis of the Brouwer diagram: in the reducing direction the materials would be better n-conductors, as more electrons would be produced.

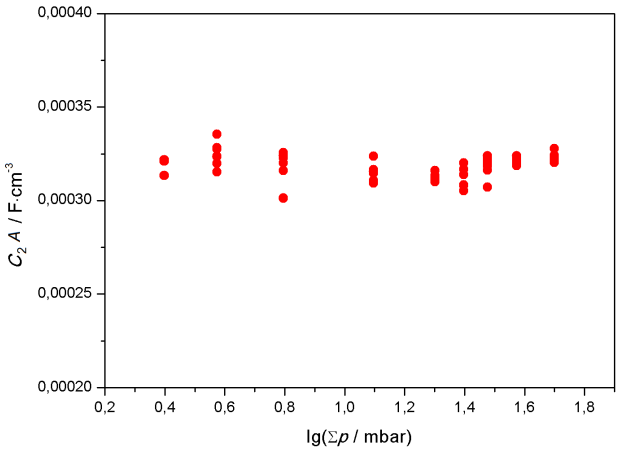

Figure 5.35: Chemical capacitance vs. total partial pressure of reaction partners (MnGDC sample, buried current collectors). One can see, that there is only statistical scattering in the values, C_2 does not depend on Σp

In these measurements the constant p_{O_2} is not necessarily guarenteed, as there could be some residual O_2 also in our diluting agent, which may be sufficient to affect the thermodynamic equlibrium of the surface reaction and therefore influence the bulk defect chemistry, and our observations might also partly be caused not only by the surface kinetics. Therefore, it should also be checked, whether the defect chemistry changes or not. To study this, one can use the chemical capacitance, which is an indicating factor for the Ce^{3+} concentration. In Figure 5.35 one can see, that the chemical capacitance is independent of Σp.

This suggests that the oxygen partial pressure is indeed constant. Also contact resistances are probably low due to the constant high-frequency intercept.

5.8 Catalytic activity depending on crystallographic orientation

The big difference between the different crystallographic planes in pure and doped ceria in respect of their surface (defect) chemistry (present ions, vacancies etc.) are expected to affect the catalytic activity. For example the (111) plane was reported to have a high amount of $V_O^{\bullet\bullet}$ on its surface [12]. In order to study this effect, additional measurements were carried out on GDC(111) and the results were compared with those obtained for GDC(100).

In this case, the electrode material was deposited on the surface of YSZ(111) single crystals. In order to investigate the orientation of the thin film, it was measured by XRD (X-ray diffraction), in $\theta - 2\theta$ geometry with a *Bruker AXS, D8 Discover* instrument. The diffractogram can be seen in Figure 5.36.

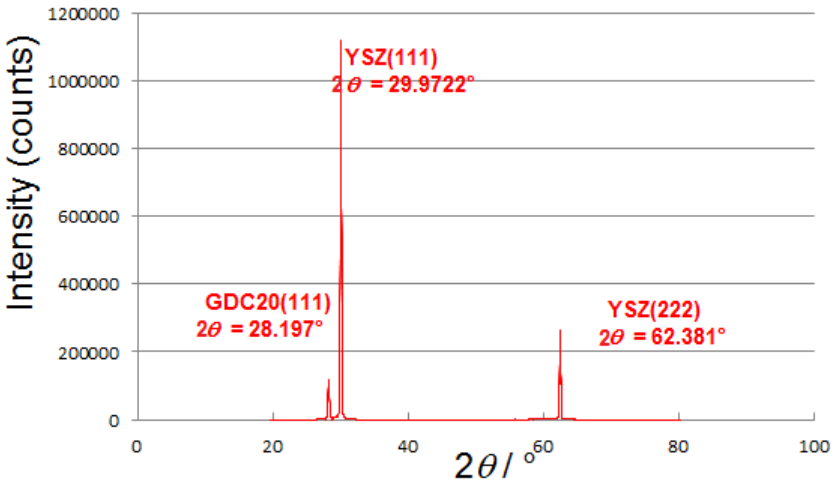

Figure 5.36: $\theta - 2\theta$ pattern of GDC grown on YSZ(111)

The diffractrogram contains only those peaks which indicate the main (111) orientation of the GDC thin film without any other orientations. Epitaxial growth of GDC on YSZ was also observed elsewhere [33].

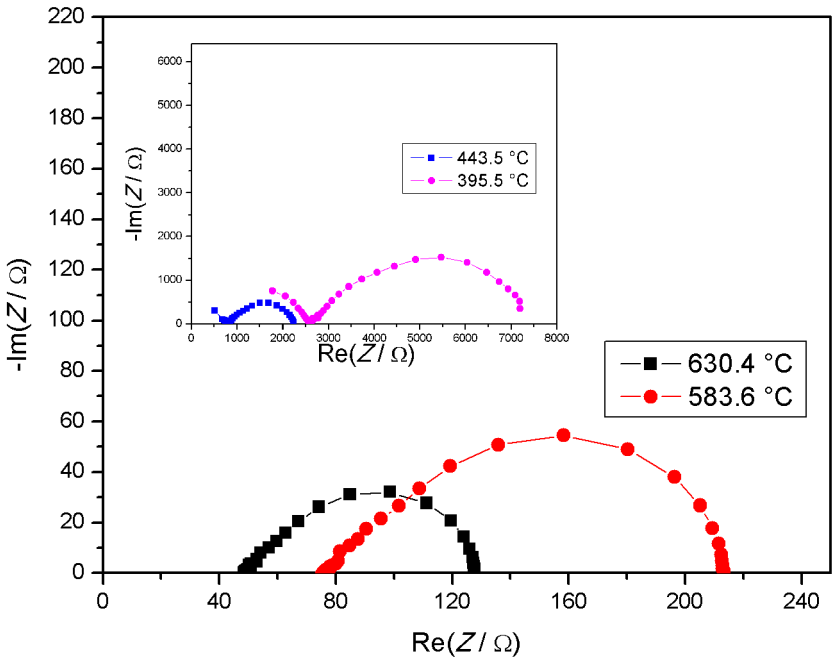

Figure 5.37: Temperature dependence of the spectra - EIS spectra measured at different temperatures (GDC(111) macro sample, buried current collectors)

Figure 5.37 illustrates the temperature dependence of the measured impedance spectra for GDC(111) macro samples. All these spectra were fitted by the simplified equivalent circuit model, shown in Figure 4.5. The appropriateness of the model for fitting is presented in Figure 5.38.

Figure 5.39 displays the resulting surface resistances for both orientations. No significant difference between the two crystallographic orientations is found, under these conditions they exhibit the same area specific resistance. This astonishing result could be interpreted by the assumption, that oxygen vacancies are not explicitly included in the

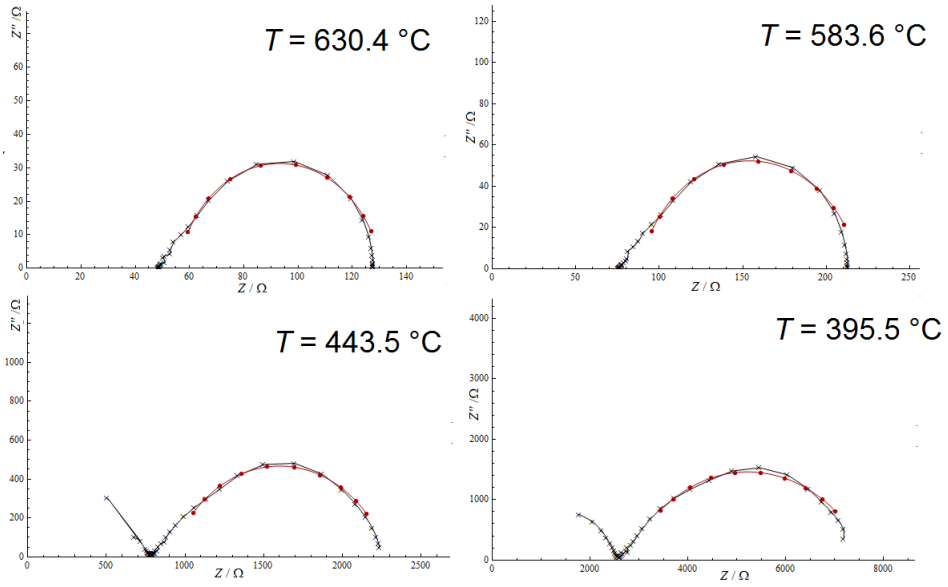

Figure 5.38: Measured spectra and their fit curves at different temperatures

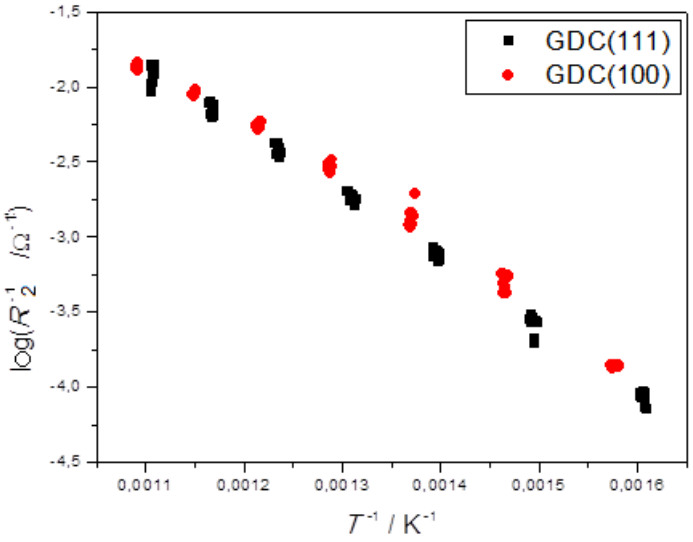

Figure 5.39: Arrhenius plots of surface resistances for GDC(111) and GDC(100) (macro measurements, metal grid beneath the electrode)

rate limiting step. Moreover, it has been discovered recently that the surface concentration of Ce^{3+} (and therefore also that of oxygen vacancies) is high also on the (100) surface, which might make the reaction rate independent of the orientation and maybe the higher oxygen vacancy concentration of the (111) surface has no significant effect on the reaction rate.

5.9 Tracer experiments, Secondary Ion Mass Spectrometry (SIMS)

For the study of the catalytic activity also tracer experiments were used. The basic idea behind this is the following: if a reaction partner taking part in a reaction occuring on the surface is marked, e.g. an isoptope is rarely present in the MIEC bulk, and one also has an isotope selective and sensitive analytical technique with high resolution, then the imaging of the reaction (rate) is possible.

In the present work, rectangular noble metal current collectors on the top and beneath of a GDC or MnGDC layer, grown on YSZ, were prepared. For comparison, also $SrTi_{0.7}Fe_{0.3}O_{3-\delta}$ was used as MIEC layer. Bottom current collectors beneath the thin film (5 nm Ti/100 nm Pt) were structured by ion beam etching, top electrodes (5 nm Cr/100 nm Au) by lift-off lithography. These samples were exposed to humidified hydrogen-argon atmosphere, which was very similar with the one used for the electrochemical measurements (same reducing conditions), but in this case with water enriched with oxygen-18 isotope (^{18}O). This atmosphere was produced by an understochiometric reaction between hydrogen and $^{18}O_2$ in a heated reaction chamber, which contained a Pt sponge. The sketch of the process can be seen in Figure 5.40: 2.5% hydrogen-containing Ar gas (Alphagaz ARCAL 10, air liquide) and the calculated quantity of oxygen-18 was introduced into the chamber in order to have $H_2^{18}O$-humidifed 2.5% hydrogen in Ar carrier gas. The stoichiometry was

checked in situ by use of a mass spectrometer (*Pfeiffer, OmniStar GSD 320*). It can be clearly seen in Figure 5.41, that after some time $I_{H_2} : I_{H^{18}O_2} \sim 1 : 1$, which corresponds to $p_{H_2} \approx p_{H^{18}O_2}$.

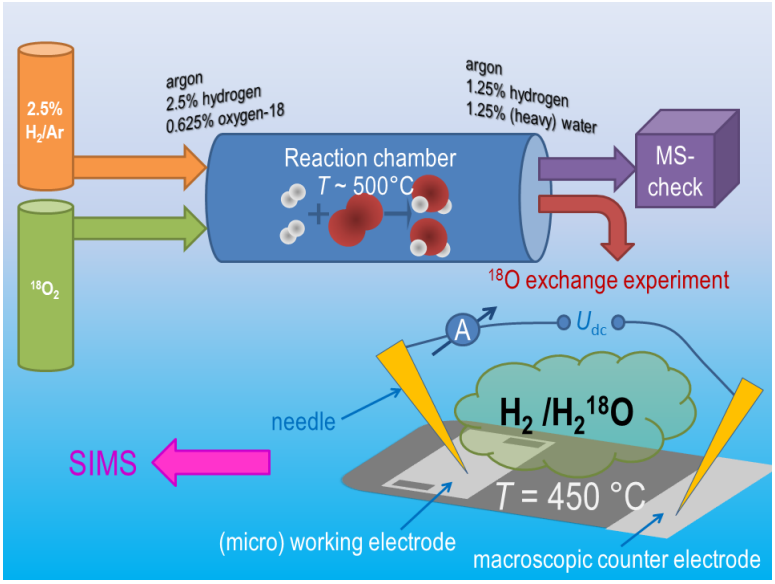

Figure 5.40: Sketch of the exchange experiment

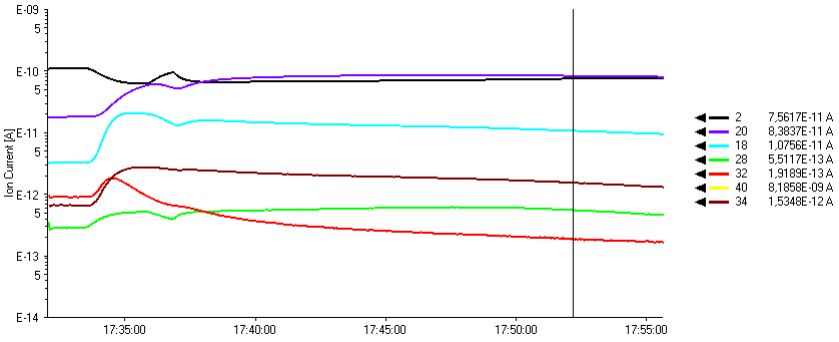

Figure 5.41: Mass spectrometric analysis of the atmosphere

The tracer experiments were performed in a closed chamber at $p = 10^5$ Pa and $T = 450$ °C set temperature, by exposing the sample to the atmosphere for a given time ($t = 10$ min). Two of the current collectors were electrically polarised against a macroscopic counter electrode (porous LSF/Pt). Without an applied bias voltage only thermal diffusion

took place (thermal equilibration), i.e., the oxygen-18 was exchanged between the solid and the atmosphere, while for the case with bias voltage also a net electrochemical reaction occured. Cathodic bias increases oxygen incorporation into the electrode, anodic bias promotes oxygen release and reduces the incorporation rate. The resulting oxygen-18 exchange was subsequently investigated by Secondary Ion Mass Spectrometry (*ToF-SIMS 5, ION-TOF GmbH, Germany*). The measurements were done in the so called CBA mode (collimated burst alignment), which allows more accurate determination of oxygen-18 in oxides [34], [35]. As primary ions, Bi_3^{2+} was used (25 kV). The negative secondary ions were then analysed in areas of 50×50 μm^2 and 160×160 μm^2, using a raster of 512×512 and 1024×1024 measurement points. For sputtering, Ce^+ ions were used (1 kV), sputter crater: 500×500 μm^2, sputtering ion current: 150 nA. The surface charging effect was compensated by use of an electron flood gun and argon flooding.

Both the oxygen-18 ions incorporated during the experiment and oxygen-16 ions which were present already before it, can be analysed. This offers the possibility of mapping of the electrochemically active zone on the electrode upon bias and of thermal oxygen diffusion properties of oxygen (without bias).

In Figure 5.42 the lateral tracer distribution in a GDC thin film is sketched. The x-axis is the distance from the current collector, while on the y-axis the tracer fraction γ can be seen:

$$\gamma = \frac{I\left(^{18}\mathrm{O}\right)}{I\left(^{16}\mathrm{O}\right) + I\left(^{18}\mathrm{O}\right)} \tag{5.36}$$

where I is the measured intensity. So, lateral distribution profiles of the isotope fraction were obtained by normalisation of the integrated intensities.

The metal layers are supposed to be blocking for oxygen ions, which was proven experimentally by measuring nearly the natural abundance tracer fraction beneath Pt electrodes in depth profiles. At first, it has to be mentioned, that even without a bias, a large amount of ^{18}O was incorporated in the material. In the zero-bias diffusion profile (red curve) a higher tracer fraction can be seen for GDC on top of the platinum electrodes. This is

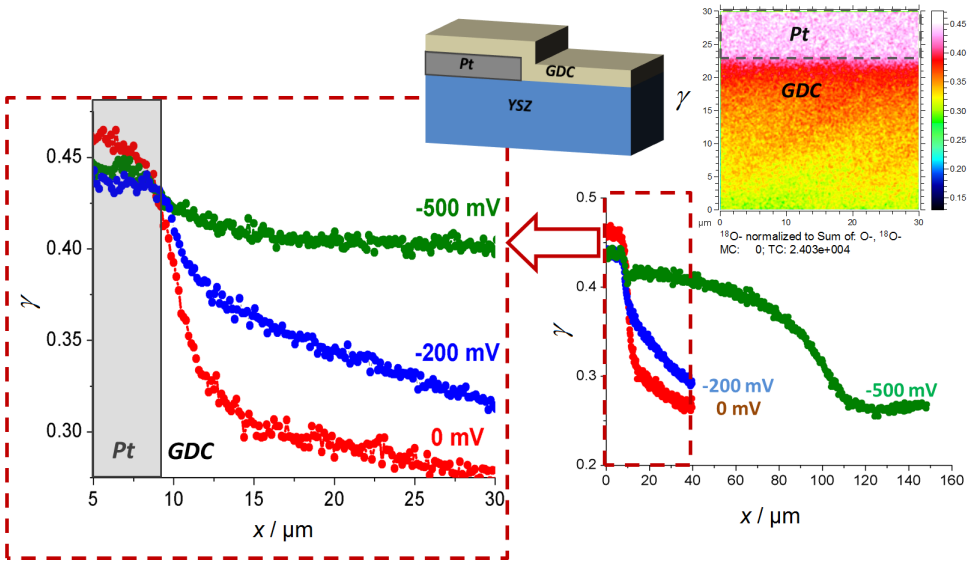

Figure 5.42: Lateral tracer distribution in a GDC thin film near a buried Pt current collector (sketch) with (-500 mV, -200 mV and wothout bias voltage (0 mV) and tracer distribution image (r.h.s. for -200 mV).

most probably caused by the blocking character of Pt. As a possibe second explanation, different surface exchange coefficients could be mentioned, however electrochemical studies do not suggest large effects on the surface kinetics, caused by substrate materials. The broadening of the concentration step width near the Pt electrode directly above YSZ can be explained by in-plane diffusion of O^{2-} ions into the electrolyte (from the region with high tracer fractions above the Pt layer). As this novel tracer experiment method was firstly used for GDC/MnGDC and STFO ($SrTi_{0.7}Fe_{0.3}O_{3-\delta}$) simultaneously in the research group [36], it is worth comparing the GDC results with the profiles of STFO. From Figure 5.43 it is obvious, that the lateral thermal profile for STFO is slightly steeper than for the GDC film. This most probably reflects the higher ionic conductivity of GDC at $T = 450$ °C compared to STFO: $\sigma_{\text{ionic, GDC}} = (3.33 \pm 0.64) \cdot 10^{-4}$ Scm^{-1}, $\sigma_{\text{ionic, STFO}} = 5.5 \cdot 10^{-6}$ Scm^{-1} [22]. These conductivity values were obtained by fitting of electrochemical measurements.

For cathodic bias, enhanced incorporation of the tracer is observable for GDC, near

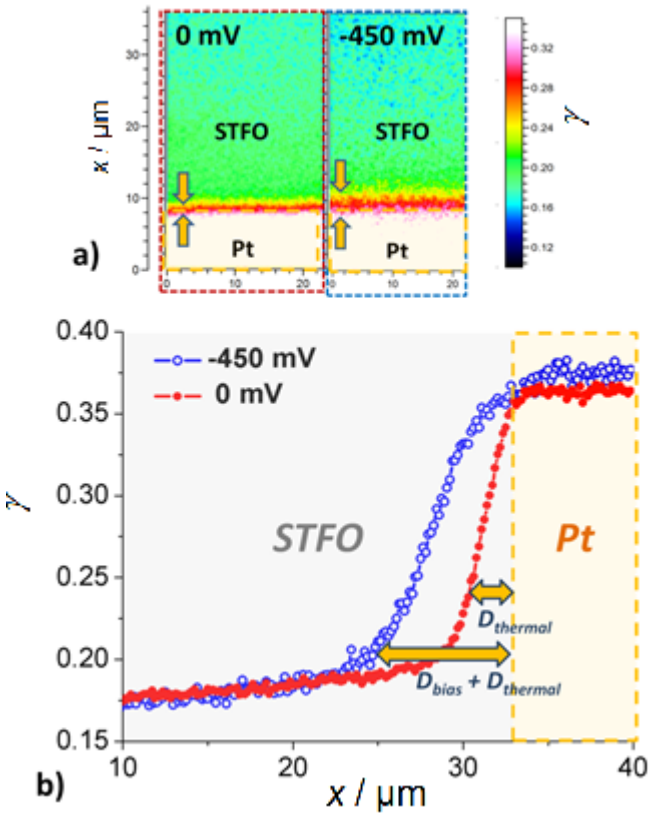

Figure 5.43: Tracer experiments on STFO electrode with (−450 mV) and without bias 0 mV a) SIMS isotope concentration images, b) lateral concentration profiles near the edge of the electrode. Electrode geometry as in Figure 5.42.

the current collector but at higher distances as well: the decay length of the electrochemically active zone is wide-spread, especially for −500 mV bias, where the width of the electrochemically active zone is drastically increased to almost 100 μm. This strong broadening is most probably caused by the severe enhancement of the electronic conductivity in cathodically polarised sample regions: cathodic bias is equivalent to a decrease in oxygen partial pressure and therefore leads to enhanced n-type electronic conductivity in the polarised region, since the defect chemistry changes, $\left[Ce^{3+}\right]$ increases (see also Section 5.4). Slight differences for the region above the Pt grid might be caused by the inhomogenity of the surface exchange coefficient or by SIMS measurement artefacts. In STFO, much less

broadening was found in the response to cathodic bias indicating a smaller width of the electrochemically active zone. This probably can be attributed to the higher electronic conductivity of GDC without bias at 700 °C ($\sigma_{\text{electronic, GDC}} = (1.19 \pm 0.26) \cdot 10^{-3}$ Scm^{-1}, $\sigma_{\text{electronic, STFO}} = (1.5 \pm 0.5) \cdot 10^{-5}$ Scm^{-1} [22] These values were obtained by fitting of electrochemical measurements.).

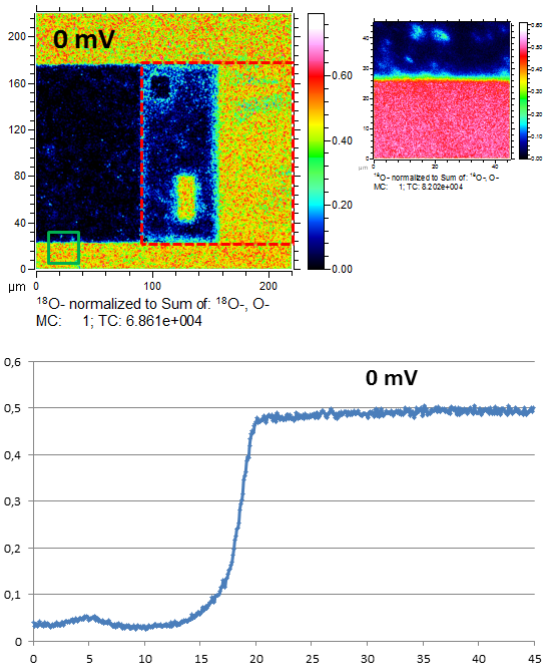

Figure 5.44: Lateral tracer distribution in a MnGDC thin film at 0 bias

For MnGDC only the experiment without bias voltage was successful. As it can be seen in Figure 5.44, the lateral thermal diffusion occurs also in MnGDC, and the broadening of the profile step is similar to GDC. This is explained by the similar ionic conductivities of the two materials ($\sigma_{\text{ionic, GDC}} = (3.33 \pm 0.64) \cdot 10^{-4}$ Scm^{-1}, $\sigma_{\text{ionic, MnGDC}} = (2.64 \pm 0.47) \cdot 10^{-4}$ Scm^{-1}. These values were obtained by fitting of electrochemical measurements.)

All these preliminary experiments clearly show the enormous potential of such tracer experiments with and without bias.

Chapter 6

Conclusions

In the present work, two ceria based materials, $Gd_{0.2}Ce_{0.8}O_{1.9-\delta}$ and $Mn_{0.1}Gd_{0.18}Ce_{0.72}O_{1.9-\delta}$ were investigated in respect of their catalytic activity for the hydrogen oxidation reaction in solid oxide fuel cells. The analysis was carried out on model-type thin film electrodes by means of several measurement techniques, with emphasis on Electrochemical Impedance Spectroscopy.

Impedance spectra were measured on microelectrodes and macroscopic electrodes. All thin film electrodes contained current collectors for a better electric contact, i.e. electron supply. The microelectrodes had two current collectors per electrode. By measuring the impedance between the two current collectors and between the microelectrode and a counter electrode, two impedance spectra were acquired. Simultaneous fitting of these spectra to specific equivalent circuits enabled the quantification of electronic and ionic conductivity, the chemical capacitance and surface catalytic activity (area specific resistance).

It was found that Gd/Mn co-doping does not increase the electronic conductivity of ceria. At lower temperatures – between $\sim$ 350 °C and $\sim$ 450 °C conductivity values of MnGDC are even slightly worse, while at higher temperature they are very similar. This might be a consequence of the additional electron trapping centres formed by the presence of Mn, which may also explain the unusually high calculated activation energy of

the polaron hopping process. All bulk properties, such as chemical capacitance and ionic conductivity are also similar with and without Mn co-doping.

The catalytic activity of MnGDC ($\sim$ inverse area specific resistance) was reproducibly found to be higher than that of GDC by a factor of ca. 2, probably due to different surface chemistry: SEM-images show significant changes on the surface of MnGDC after tempering at 700 °C in reducing atmosphere. Furthermore, time dependent experiments showed that MnGDC exhibits interesting variations: the surface activity increases during the first 5 hours, and subsequently degrades in a micro measurement setup. Macro measurements exhibited much slower degradation.

Impedance measurements carried out with bias proved, that the defect concentration in the materials can be varied by applied overpotential, which is equivalent to a change in the partial pressure of oxygen. Tracer exchange experiments were also performed in order to monitor the oxygen exchange of the electrodes. The electrochemically active zone could be visualised by comparing thermal and bias-driven tracer exchange.

List of Figures

List of Tables

Bibliography

[1] S.C. Singhal. Solid oxide fuel cells for stationary, mobile, and military applications. *Solid State Ionics*, 152–153(0):405 – 410, 2002.

[2] N.Q. Minh. Ceramic fuel cells. *Journal of the American Ceramic Society*, 76(563-588), 1993.

[3] A. Opitz. Technology of functional materials. University Lecture, 2013.

[4] R.M. Ormerod. Solid oxide fuel cells. *Chemical Society Reviews*, 32:17–28, 2003.

[5] R.J. Gorte and J.M. Vohs. Novel SOFC anodes for the direct electrochemical oxidation of hydrocarbons. *Journal of Catalysis*, 216(1–2):477 – 486, 2003.

[6] C. Lu, W.L. Worrell, C. Wang, S. Park, H. Kim, J.M. Vohs, and R.J. Gorte. Development of solid oxide fuel cells for the direct oxidation of hydrocarbon fuels. *Solid State Ionics*, 152–153:393 – 397, 2002.

[7] Direct oxidation of hydrcarbons in solid oxide fuel cell.

[8] T. Zhang, L. Kong, Z. Zeng, H. Huang, P. Hing, Z. Xia, and J. Kilner. Sintering behavior and ionic conductivity of $Ce_{0.8}Gd_{0.2}O_{1.9}$ with a small amount of MnO_2 doping. *Journal of Solid State Electrochemistry*, 7(6):348–354, 2003.

[9] J. Fleig, F. S. Baumann, V. Brichzin, H. R. Kim, J. Jamnik, G. Cristiani, H. U. Habermeier, and J. Maier. Thin Film Microelectrodes in SOFC Electrode Research. *Fuel Cells*, 6:284–292, 2006.

[10] R.J.D. Tilley. *Understanding Solids: The Science of Materials*. Wiley, 2005.

[11] W.C. Chueh and S. M. Haile. A thermochemical study of ceria: Exploiting an old material for new modes of energy conversion and CO_2 mitigation. *Philosophical Transactions of the Royal Society: Mathematical, physical and engineering sciences*.

[12] M.S. Kozlov and K.M. Neyman. O vacancies on steps on the $CeO_2(111)$ surface. *Physical Chemistry Chemical Physics*, 16:7823–7829, 2014.

[13] M.G. Norton C.B. Carter. *Ceramic materials: Science and Engineering*. Springer Verlag, 2013.

[14] `http://www.numis.northwestern.edu/404/Lectures_12/Pointdefectslecturefor404.pdf`. Accessed: 2014-06-10.

[15] G. Cai, R. Liu, C.Zhao, J. Li, S. Wang, and T. Wen. Anode performance of mn-doped ceria–scsz for solid oxide fuel cell. *Journal of Solid State Electrochemistry*, 15:147–152, 2011.

[16] CH.Y. Kang, H. Kusaba, H. Yahiro, K. Sasaki, and Y. Teraoka. Preparation , characterization and electrical property of mn-doped ceria-based oxides. *Solid State Ionics*, 177:1799–1802, 2006.

[17] WTWA-Praktikum. based on the "Kurze Einleitung in Impedanzspektroskopie" guide. MSc Labor Pracice, 2013.

[18] S.B. Adler, X.Y. Chen, and J.R. Wilson. Mechanisms and rate laws for oxygen exchange on mixed-conducting oxide surfaces. *Journal of Catalysis*, 245(1):91 – 109, 2007.

[19] 01-075-0162. ICDD (2010). PDF-4+ 2010 (Database), edited by Dr. Soorya Kabekkodu, International Centre for Diffraction Data, Newtown Square, PA, USA.

[20] A. Opitz. Die Kinetik der Sauerstoffreduktion an mikrostrukturierten Platinschichten auf Yttrium stabilisiertem Zirconiumoxid. Masters Thesis, Vienna University of Technology, 2008.

[21] T. Huber. Konstruktion einer Vakuum Mikrokontaktapparatur und Impedanzmessungen an mikrostrukturierten Platin- und Nickelelektroden auf Yttrium Stabilisiertem Zirconiumoxid in Wasserstoff Atmosphaere. Masters Thesis, Vienna University of Technology, 2010.

[22] A. Nenning. Electrochemical reactions and transport paths of $SrTi_{0.7}Fe_{0.3}O_{0.3-\delta}$ thin film model electrodes in H_2 - H_2O atmosphere. Master's thesis, Vienna University of Technology, 2012.

[23] J. Fleig. On the current-voltage characteristics of charge transfer reactions at mixed conducting electrodes on solid electrolytes. *Physical Chemistry Chemical Physics*, 7:2027–2037, 2005.

[24] W.C. Chueh and S.M. Haile. Electrochemical studies of capacitance in cerium oxide thin films and its relationship to anionic and electronic defect densities. *Physical Chemistry Chemical Physics*, 11:8144–8148, 2009.

[25] E. Ruiz-Trejo and J. Maier. Electronic transport in single crystals of gd-doped ceria. *Journal of the Electrochemical Society*, 154:583–587, 2007.

[26] W.C. Chueh and S.M. Haile. Electrochemistry of mixed oxygen ion and electron conducting electrodes in solid electrolyte cells. *Annual Review of Chemical and Biomolecular Engineering*, 3.:313–341, 2012.

[27] J.F. Steven. *Byrnes Department of Physics, University of California at Berkeley, Berkeley.* CA 94720 December 2, 2008.

[28] J.T. Devreese. Polarons. *Polarons in Digital Encyclopedia of Applied Physics, edited by G.L. Trigg*, 2008.

[29] J. Jamnik and J. Maier. Generalised equivalent circuits for mass and charge transport: chemical capacitance and its implications. *Physical Chemistry Chemical Physics*, 3(1668-1678), 2001.

[30] T. Holstein. Studies of polaron motion: Part ii. the "small" polaron. *Annals of Physics*, 8(3):343 – 389, 1959.

[31] L. Friedman and T. Holstein. Studies of polaron motion: Part iii: The hall mobility of the small polaron. *Annals of Physics*, 21(3):494 – 549, 1963.

[32] R.A. Marcus. Chemical and Electrochemical Electron-Transfer Theory. *Annual Review of Physical Chemistry*, 15:155–196, October 1964.

[33] W.C. Chueh, Y. Hao, W. Jung, and S.M. Haile. High electrochemical activity of the oxide phase in model ceria-Pt and ceria-Ni composite anodes. *Nature Materials*, 11:155–161, 2011.

[34] G. Holzlechner, M. Kubicek, H. Hutter, and J. Fleig. A novel tof-sims operation mode for improved accuracy and lateral resolution of oxygen isotope measurements on oxides. *Journal of Analytical Atomic Spectrometry*, 28:1080–1089, 2013.

[35] M. Kubicek, G. Holzlechner, A.K. Opitz, S.Larisegger, H.Hutter, and J.Fleig. A novel tof-sims operation mode for sub 100xa0;nm lateral resolution: Application and performance. *Applied Surface Science*, 289(0):407 – 416, 2014.

[36] A. Nenning, E. Navickas, P. Velicsanyi, A.K. Opitz, H. Hutter, and J. Fleig. Mapping of surface exchange of mixed conducting $Sr(Ti_{0.7}Fe_{0.3})O_3$ and $Ce_{0.8}Gd_{0.2}O_{1.9}$ thin films by ^{18}O tracer incorporation under reducing atmosphere. submitted 2014.